



# IMAGING TECHNIQUES FOR INTRAOPERATIVE VISUALISATION OF LOW GRADE GLIOMAS



24-06-2015

TECHNISCHE GENEESKUNDE

BACHELOR 3

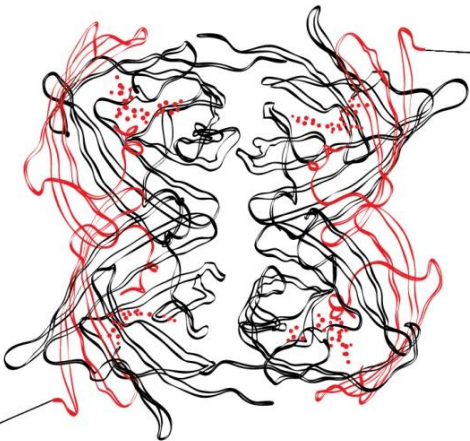
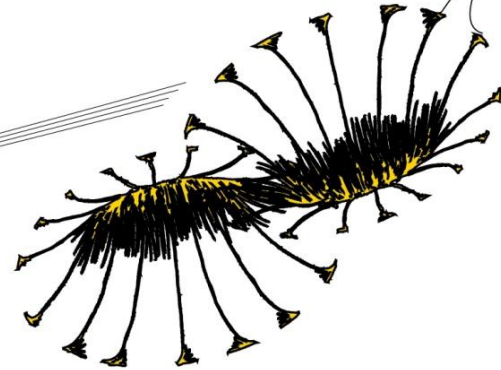
MDO

SUPERVISORS:

MD. PhD. M. TER LAAN

PROF. DR. IR. W. STEENBERGEN

L. VOSKUILEN



Lotte van Dongen  
Klijs de Koning  
Samantha Noteboom  
Lisette Raasing

# Table of contents

<b>1</b>	<b>Introduction</b> .....	<b>3</b>
<b>2</b>	<b>Requirements</b> .....	<b>5</b>
<b>2.1</b>	<b>Absolute requirements</b> .....	<b>5</b>
<b>2.2</b>	<b>Relative requirements</b> .....	<b>6</b>
<b>3</b>	<b>Properties of low grade glioma</b> .....	<b>7</b>
<b>4</b>	<b>Selection of imaging techniques</b> .....	<b>9</b>
<b>4.1</b>	<b>Evaluation of rejected techniques</b> .....	<b>10</b>
4.1.1	Photodynamic Diagnosis.....	10
4.1.2	3D Ultrasound .....	10
4.1.3	Photoacoustic Imaging.....	10
4.1.4	Narrow Band Imaging .....	10
4.1.5	Confocal Microscopy.....	10
4.1.6	Desorption Electrospray Ionization Mass Spectrometry .....	11
<b>4.2</b>	<b>Included imaging techniques</b> .....	<b>12</b>
4.2.1	Hyperspectral Imaging .....	12
4.2.2	Optical Coherence Tomography .....	17
4.2.3	Optical coherence Elastography .....	22
4.2.4	Infrared Spectroscopy.....	26
4.2.5	Nonlinear Microscopy.....	29
4.2.6	Raman Spectroscopy.....	33
<b>5</b>	<b>Comparison of included imaging techniques</b> .....	<b>37</b>
<b>5.1</b>	<b>Sensitivity and specificity</b> .....	<b>38</b>
<b>5.2</b>	<b>Field of view</b> .....	<b>38</b>
<b>5.3</b>	<b>Level of development</b> .....	<b>39</b>
<b>5.4</b>	<b>Applicability in the OR</b> .....	<b>39</b>
<b>5.5</b>	<b>Implementation into the OR-microscope</b> .....	<b>40</b>
<b>6</b>	<b>Experiments</b> .....	<b>41</b>
<b>6.1</b>	<b>Optical Coherence Tomography</b> .....	<b>41</b>
<b>6.2</b>	<b>Hyperspectral Imaging</b> .....	<b>44</b>
<b>6.3</b>	<b>Near-infrared Spectroscopy</b> .....	<b>47</b>
<b>6.4</b>	<b>Fluorescence Spectrometry</b> .....	<b>50</b>
<b>7</b>	<b>Discussion and conclusion</b> .....	<b>52</b>
<b>8</b>	<b>References</b> .....	<b>54</b>

# Abstract

Surgical treatment of low-grade gliomas (LGGs) aims for maximal removal of tumour tissue, while minimising the risk of damaging functional areas. LGG is hard to distinguish from healthy brain tissue during surgery and for safe resection a part of the tumour is left behind. To improve the extent of resection (EOR), a new approach of imaging is required to visualise LGGs intraoperatively. This paper presents an overview of imaging techniques, which could be suitable for this purpose. Absolute requirements were determined and used to select imaging techniques. Included imaging techniques were graded based on relative requirements. In addition to literature study, exploratory experiments were performed with promising techniques. Ultimately, a comparison of the considered techniques was arranged to make a recommendation. Hyperspectral imaging (HSI) seemed most promising followed by Raman Spectroscopy (RS). Optical Coherence Tomography (OCT), Optical Coherence Elastography (OCE), Infrared Spectroscopy (IRs) and Nonlinear Microscopy also showed potential for intraoperative visualisation of LGGs.

## 1 Introduction

Gliomas are tumours originating from glial cells in the brain. Four types of glial cells can be distinguished: astrocytes, oligodendrocytes, microglia and ependymal cells. Those cells can respectively lead to astrocytoma, oligodendroglioma, oligoastrocytoma and ependymoma, respectively(1). The World Health Organisation (WHO) classification system categorises gliomas in grade one till four (see table 1). Grade I and II tumours are termed low grade gliomas (LGGs), while grade III and grade IV are termed high grade gliomas (HGGs) (see *table 1*). Since intraoperative visualisation of LGG tissue is hard compared to HGG visualisation, the main focus of this paper will be on LGG grade II. These include astrocytomas, oligodendrogliomas and oligoastrocytomas (*table 1*). Ependymomas are excluded because of their well determined location around the ventricles and their low prevalence(2).

WHO classification	Type
<b>Grade I:</b>	Pilocytair astrocytoma Piloxyoid astrocytoma
<b>Grade II:</b>	Diffuse low grade astrocytoma Diffuse low grade oligodendroglioma Diffuse low grade oligoastrocytoma (mixed-glioma) Ependymomas
<b>Grade III:</b>	Anaplastic astrocytoma Anaplastic oligodendroglioma Anaplastic oligoastrocytoma (mixed glioma) Gliomatosis cerebri
<b>Grade IV:</b>	Glioblastoma multiforme (GBM)

**Table 1** WHO classification system gliomas

Patients diagnosed with WHO grade II glioma have an expected survival rate of 5-10 years (3). After diagnosis of LGG, either watchful waiting or treatment can be chosen. Watchful waiting is only recommended in low-risk patients with minimal or no symptoms. Untreated LGGs will inevitably propagate to HGGs (4). Currently, the best treatment for LGG is surgical resection. Radiotherapy and chemotherapy are other possible treatments, but show no or little improvement of overall survival (5, 6). Studies increasingly support surgical removal rather than watchful waiting to improve overall

survival, provided that the tumour is operable (7). Unfortunately, the infiltrative diffuse character of LGGs makes complete removal impossible (8, 9), and almost all patients will suffer from a recurrent tumour after resection (10),(11),(12),(13),(14).

Studies have shown that more extensive surgical resection improves overall patient survival and provides a longer time window before the tumour propagates to a higher grade (14, 15). Nevertheless, LGGs are removed carefully, because no functional brain tissue should be removed. This way parts of the tumour are always left behind (16). As a consequence, surgical removal of LGGs presents a challenge: removing as much tumour tissue as possible without damaging any functional brain areas (16).

The current method of LGG surgery implies a preoperatively MRI scan to determine the location of the tumour. During surgery, LGG resection can be improved using MRI-guided neuronavigation and ultrasound (17). However, both methods have their limitations. Brain swelling and surgical removal lead to intraoperative deformation of the brain, which is called brain shift. As a consequence, the accuracy of neuronavigation decreases during surgery and is most unreliable in the final stages of tumour removal (18). Intraoperative ultrasound also has important disadvantages. The OR-microscope has to be put aside to place the ultrasound probe on the tissue. After imaging the tumour, the surgeon has to remember the location and put the OR-microscope back before continuing the operation.

For HGGs an additional tool is developed to overcome these limitations. 5-aminolevulinic acid (5-ALA) can be used as a contrast agent to image the HGG intraoperatively (8). Healthy brain tissue is able to degrade this contrast agent. HGG tissue on the other hand, is too much dedifferentiated and not able to degrade 5-ALA. Hence, 5-ALA is absorbed in HGG cells, which causes fluorescence by certain wavelengths of light. LGGs are less dedifferentiated than HGGs, and are able to degrade the 5-ALA. In this way, 5-ALA cannot make a contrast between healthy brain tissue and LGG (19). Since 5-ALA is not able to visualise LGG, it is up to the surgeon to distinguish the tumour from functional brain tissue using the OR microscope and his own eyes. Unfortunately, low grade gliomas are difficult to discriminate from normal tissue macroscopically. There is no imaging technique available yet capable of visualising an entire LGG intraoperatively, while a greater extent of resection (EOR) is very important for overall patient survival (14, 15). This means a new imaging technique is required to visualise LGGs, so a bigger part can be removed without damaging the functional areas of the brain.

The goal of this research paper is to find an imaging technique which can distinguish LGG tissue from healthy brain tissue intraoperatively. In order to select suitable techniques, absolute and relative requirements are determined to which the imaging techniques must comply. Furthermore LGG tissue properties determined by several (diagnostic) techniques are listed. Based on the absolute requirements and their ability to distinguish LGG from healthy brain tissue, a couple of imaging techniques will be selected. These techniques will be further investigated and graded based on the relative requirements. Ultimately the imaging techniques will be compared to each other, and graded based on the relative requirements. This will result in a survey of imaging techniques which seem promising for the intraoperative visualisation of LGG. Based on the given grades, a recommendation could be made which technique is most suitable. Alongside the literature study, ex vivo experiments will also be performed on both HGG and LGG samples. A couple of imaging techniques that seem promising will be tested, to see if a distinction can be made.

## 2 Requirements

Techniques included in this research should be able to image the characteristics of a LGG, so it is possible to distinguish LGG from healthy brain tissue. To further select suitable imaging techniques, requirements are determined and divided in two subcategories. The first category is the absolute requirements to which the techniques definitely should comply to. When a technique does not comply with all of the absolute requirements it will be excluded from this research. The second category consists of the relative requirements. These requirements will be used to grade the techniques which comply with the absolute requirements. The requirements are relative, because improvement may be possible. This means an imaging technique could still be useful, even if it does not fully comply to the relative requirements at the moment. An overview of the requirements is shown in *table 2*.

<b><i>Absolute requirements</i></b>	<b><i>Relative requirements</i></b>
Real-time	High sensitivity and specificity
In vivo	Applicability in the OR
No brain contact	Field of view
No tissue damage	Level of development
No contrast agent	Implementation into the OR

**Table 2** Overview of the absolute and relative requirements for selecting suitable techniques

### 2.1 Absolute requirements

The first absolute requirement is real-time imaging, which is essential for intraoperative use. The surgery should not be interrupted for imaging and the surgeon has to immediately see the difference between the tumour and healthy brain tissue.

Secondly, in vivo scanning of the tissue should be possible. If no in vivo images can be made, trying to implement the technique during surgery is pointless. Some techniques require pre-processing of tissue samples. This way those techniques are only able to be applied on ex vivo tissue.

Furthermore, the technique should be able to make images without any brain contact. If the surgeon would have to switch between the OR microscope and some kind of probe, the technique would not be an improvement compared to the existing methods like intraoperative ultrasound.

Moreover, the technique should not cause any damage to the brain. Working with a technique, which might cause brain damage, is out of the question.

The final absolute requirement is: no contrast agent is needed. This should be avoided because of possible side effects and high costs.

## 2.2 Relative requirements

First of all, a high sensitivity and specificity is the most important relative requirement. A new imaging technique should be able to distinguish the LGG from the healthy tissue in a reliable way. Otherwise, it would come with too many risks. The specificity is most important, because absolutely no healthy tissue should be marked as tumour tissue. Since sensitivity and specificity are dependent of the application, it is not possible to determine this requirement when a technique is not applied on brain tissue yet. This is why sensitivity and specificity is not an absolute requirement, but will be determined on its potential.

The second relative requirement is applicability in the OR. This is important because a new imaging technique for intraoperative use should be able to be applied into the OR. When for some techniques this appears to be impossible, the limitations should be solved.

The field of view (FOV) is an important relative requirement. The FOV has to be at least 1 cm<sup>2</sup>, in combination with a high resolution, because resection of the LGG takes place in order of multiple centimetres. Lower FOV would limit the surgeon's ability to see the full resection plane. The reason why FOV is not an absolute requirement is because the FOV could be enlarged for some techniques in order to make those suitable for LGG resection.

Level of development is also a relative requirement. For example, some techniques are already implemented in the OR, while other techniques require a lot of adjustments before implementation is possible. The techniques which are already implemented in the OR are more suitable for the application at this moment.

Implementation into the OR microscope is the last relative requirement. Since LGG surgery always requires the use of an OR-microscope, the new imaging device should be able to be integrated into the microscope. This way the imaging device achieves optimal ease of use.

### 3 Properties of low grade glioma

LGG cells are relatively less dedifferentiated from normal glial cells. Hereby, LGG tissue shows many similarities to healthy brain tissue and some glioma cells are even still functional. Moreover, LGGs show no increase in angiogenesis or mitotic activity (20, 21). These factors complicate distinguishing LGG from healthy brain tissue. Another factor which complicates detection of LGG is that it forms a heterogeneous group of cells (9). LGGs contain different cell types with different properties so no overall characteristic can be found to distinguish them. This wide range of properties logically result in a wide range of appearances for glial originated tumours (22). Despite the described limitations, the following techniques are currently able to distinguish LGG from healthy brain tissue based on different characteristics.

Magnetic resonance imaging (MRI) is a highly sensitive test to diagnose LGG. LGG appears as a low-intensity area on T1-weighted images, which suggest a low lipid concentration of LGG compared to healthy brain tissue. In contrast to T1, an increase in signal intensity is seen in T2-weighted images which represent a higher water density. The lesion usually presents as a homogeneous area without necrosis(23). Other forms of MRI are also promising in detecting LGG based upon different tissue properties. Diffusion-weighted MRI (DWI) is a form of MRI which reflects the mobility of water molecules in tissue. The apparent diffusion coefficient (ADC) shows the value of the magnitude from diffusion of water in tissue, and is mainly determined by the density of cells. Hyper cellular tumours have a relatively low ADC and a high signal on the DWI. A study by Khayal et al, 2011 showed low grade astrocytomas had higher ADC values on the DWI than low grade oligodendrogliomas(24). According to Lee et al, 2008, "hot spots" with a low ADC can be shown in the brain using DWI, which are presumed to be low grade astrocytoma(25). Perfusion weighted MRI can be used to measure the relative cerebral blood volume (rCBV). A study by Cha et al. has shown the rCBV is variably abnormal in astrocytomas. Moreover oligodendrogliomas show a higher rCBV than astrocytomas(26). Based on rCBV, distinction between LGG tissue and healthy brain tissue might be made(27). Perfusion weighted MRI has already been used to find spots of anaplastic glioma(28). Moreover, higher rCBVs in LGG have been associated with a shorter time of tumour progression to a higher grade(29, 30).

Magnetic resonance spectroscopy imaging (MRSI) detected a difference in myoinositol level of LGG tissue compared to healthy brain tissue. There has been proven that myoinositol is elevated in LGG tissue and demyelinating lesions. Myoinositol is considered to be a marker of glial cells and is located in astrocytes. Studies have shown that myoinositol is elevated in astrocytomas and its concentration decreases when malignancy increases(31). The N-acetylaspartate (NAA)/ creatine ratio (NAA/CR) is another marker detected by MRSI which is decreased in LGG.

Computed tomography (CT) images LGG as an area with the same or lower density than the surrounding brain and no enhancement(23).

Ultrasound shear wave elastography showed LGGs have a mean elasticity of  $23.7 \pm 4.9$  kPa, while normal brain tissue has a mean elasticity of  $7.3 \pm 2.1$  kPa, which implicates LGGs are significantly stiffer than healthy brain tissue(32). *Figure 1* shows the different elasticities from different kinds of brain tumours compared to healthy brain tissue.

The described techniques were able to image LGG based on different characteristics, but were excluded in this research (see following chapter). However, some characteristics can be used as a base by selecting other techniques. The indicated properties have already shown being useful for making contrast of LGG and this way could be considered as contrast mechanism for other techniques.

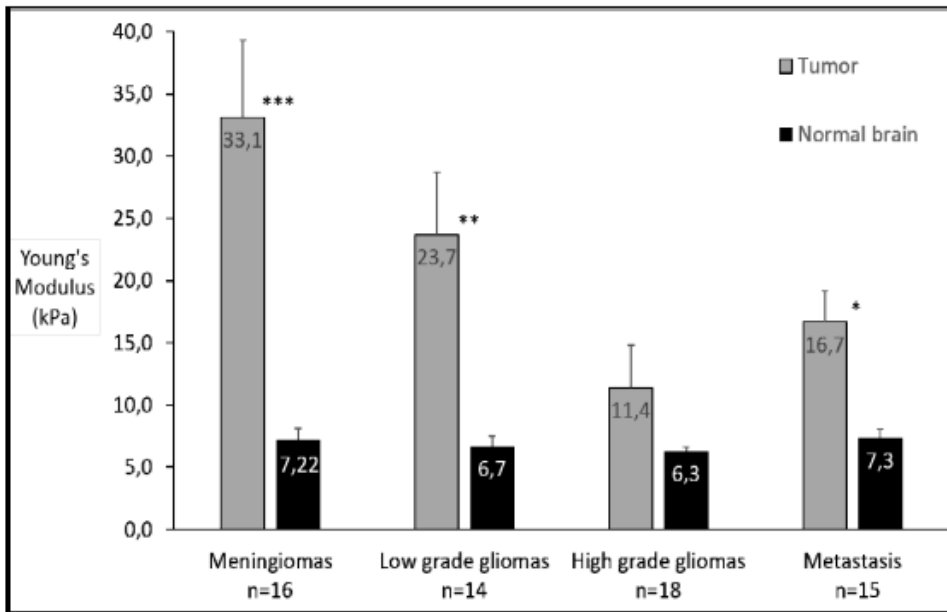


Figure 1 Elasticity properties of brain tumours

## 4 Selection of imaging techniques

The first phase of this study was exploring which imaging techniques could theoretically be suitable for detecting LGGs intraoperatively. All techniques that are only able to obtain data from electro-neurophysiological processes in the brain, e.g. electroencephalography (EEG) and magnetoencephalography (MEG), were excluded from further research immediately. These techniques are only able to produce data of physiological processes, and not of anatomical structures. Since little dedifferentiated glioma cells still show neurophysiological processes, these cells will not be detected using such an imaging technique and so this would still limit the EOR. Conventional techniques used in preoperative imaging like Computed Tomography (CT), Magnetic Resonance Imaging (MRI), Single Proton Emission Computed Tomography (SPECT) and Positron Emission Tomography (PET) were excluded as well, because it was known in advance they would not comply to the absolute requirements. These techniques cannot operate in real-time, or require ionizing radiation to produce images. Techniques which are very expensive or impractical to apply in the OR, was another reason to reject these instantly.

As previously mentioned, the remaining techniques will be analysed based on absolute requirements. The techniques which do not comply with the absolute requirements will be discussed briefly and are further excluded from this research. Subsequently, the included techniques will be discussed more extensively and evaluated based on the absolute and relative requirements. The results of the selected techniques are given in an overview shown in *table 3*.

<b>Instantly excluded imaging techniques</b>	<b>Excluded imaging techniques based on absolute requirements</b>	<b>Included imaging techniques</b>
Computer Tomography (CT)	Photodynamic Diagnosis (PDD)	Hyperspectral Imaging (HSI)
Magnetic Resonance Imaging (MRI)	(3D) Ultrasonography (US)	Optical Coherence Tomography (OCT)
Positron Emission Tomography (PET)	Photoacoustic Imaging (PI)	Optical Coherence Elastography (OCE)
Single Photon Emission Computed Tomography (SPECT)	Narrow Band Imaging (NBI)	Infrared Spectroscopy (IR)
Electroencephalogram (EEG)	Confocal Microscopy (CM)	Nonlinear Microscopy (NM)
Magnetoencephalogram (MEG)	Desorption Electrospray Ionisation Mass Spectroscopy (DESI-MS)	Raman Spectroscopy (RS)

**Table 3 overview of imaging techniques**

## 4.1 Evaluation of rejected techniques

### 4.1.1 Photodynamic Diagnosis

This imaging device is based on fluorescence and can be used in fluorescence guided surgery in malignant brain tumours. This fluorescence is based on the broken blood-brain barrier in malignant tumours which results in accumulation of fluorescent dye. Since low-grade tumours still have their blood-brain barriers intact, fluorescent dye will not accumulate. Thus, this technique cannot distinguish LGG tissue from healthy brain tissue. Furthermore, this technique is based on photodynamic therapy and may be harmful for normal neural and glial cells(33). Based on these facts, this technique is not worth investigating more extensively.

### 4.1.2 3D Ultrasound

Ultrasound (US) can be used during LGG surgery to improve imaging of glioma boundaries. Furthermore it can be used for imaging HGGs as well. It seems to be a promising technique, because it is able to image the low grade glioma real-time, *in vivo*, without damaging the tissue or using a contrast agent. However this technique does not improve the results compared to MRI guided neuronavigation. In addition, US can only produce images when physical contact is made with investigated tissue (34).

### 4.1.3 Photoacoustic Imaging

Photoacoustic imaging (PI) does not comply to the requirements, because tissue contact is required to image. Noncontact piëzo-electric detection of photo acoustic signals might be able to overcome this problem (35). Air-coupled ultrasound transducers allow noncontact imaging, when placed above the tissue with an air gap of 7.5 mm. This technique detects malignant tissue by the presence of enlarged blood concentrations due to increased vascularisation. Since angiogenesis has not been taken place in LGGs, this cannot be used as a contrast mechanism in grade II gliomas (36).

### 4.1.4 Narrow Band Imaging

Narrow band imaging (NBI) uses small bands of different wavelengths, usually green or blue, to detect differences in tissue. It is possible to use NBI for real time, *in vivo* imaging. In a study by Singh et al. 2013 the researchers used NBI to predict the histology of colorectal polyps in real-time during a colonoscopy. They graded the polyps. These were subsequently removed by biopsy or surgically. The NBI system was integrated with the endoscope(37). Sasagawa et al. used a scope with a built in NBI system for Intra- and paraventricular brain tumour biopsies. The tumour tissue appeared to be a cyan colour under the NBI laser, which made it distinguishable from normal tissue. The probe was navigated into the brain, but the tumour tissue did not have to be touched to be recognised(38). In none of the studies a contrast agent was used and no brain damage reported in any of the cases. It is more difficult to prove if LGGs could be detected using NBI, because this has not been done before. NBI is used to detect differences in vascularisation (39). However, this is however not relevant for LGGs, as they do not have an increased vascularisation. Therefore this technique is not suitable for the resection of gliomas.

### 4.1.5 Confocal Microscopy

Confocal microscopy (CM) is a microscopic technique which uses a pinhole to enhance contrast and resolution, a small part of the tissue sample is illuminated at the same time, to avoid light pollution(40). CM is used to make images *in vivo*. For example, *in vivo* examination of melanomas has been made using CM laser scanning (41). In another study, researchers tried to visualise brain tumours. This included real-time surgery of LGGs. A reduced confocal microscope scanner encased in a rigid probe was used to scan tumours. However, the FOV was very small and a contrast agent was used in this case. Differences between low grade astrocytomas, and oligodendrocytomas and normal brain tissue could be visualised (42). Articles where confocal microscopy was used without any

contrast agent were not found. This makes confocal microscopy a technique which does not meet the requirements.

#### 4.1.6 Desorption Electrospray Ionization Mass Spectrometry

Different forms of mass spectroscopy are secondary ion mass spectrometry (SIMS), matrix-assisted laser desorption ionization mass spectrometry (MALDI-MS) and desorption electrospray ionization mass spectrometry (DESI-MS) (43). DESI-MS has already been used intraoperatively during breast cancer surgery to distinguish tumour tissue from healthy breast tissue based on differences in lipids. During this surgery real-time imaging of DESI-MS was possible (44). Mass-spectrometry imaging can distinguish proteins, lipids and metabolites without using contrast agent. DESI-MS also allows direct tissue analysis without sample preparation and can be used in vivo (45). In glioblastomas DESI-MS has been proven promising to distinguish tumour tissue from brain tissue intraoperatively and to grade the tumour. However, this method is based on image guided needle biopsies. This is the main disadvantage of DESI-MS, namely the molecules always need to leave the tissue for MS analysis (46). This fact is in contrast with the requirements of no brain contact and no tissue damage, so no further investigation is needed.

## 4.2 Included imaging techniques

### 4.2.1 Hyperspectral Imaging

Spectral imaging can be used to collect spectral information from a sample. This information can be used for different applications. Several spectral imaging techniques are available, which differ in number of wavelength bands and precision. Hyperspectral imaging (HSI) can detect more wavelength bands along a larger spectral range, which results in higher accuracy compared to conventional spectral imaging. *Table 4* shows the differences between the different spectral imaging devices (47).

Spectral imaging	Fresse et al. <sup>12</sup>		Puschell <sup>1</sup>	
	Band no.	Precision ( $\Delta\lambda/\lambda$ )	Band no.	Resolution (nm)
Multispectral	5 to 10	0.1	Order of 10	~ 20 to 100
Hyperspectral	100 to 200	0.01	~ 30 to 300	< 10
Ultraspectral	1000 to 10,000	0.001	> 300	< 1

**Table 4 Differences in specifications between multi-, hyper- and ultraspectral imaging**

The spectrometer is built from three main components: a light source, a spectral separator and a detector. Light is sent into the investigated tissue. After entering the tissue the light will be reflected, absorbed or transmitted. The spectrometer uses the reflected light as the source of information. The reflected light passes the spectral separator which divides the light into several spectral bands. Finally, the detector measures these spectral bands and transfers them to a computer which processes this data. This process is shown in *figure 2* (48) Spatial data obtained with HSI can give information about tissue morphology, physiology and composition. As a result of disease, tissue will change which can be detected using HSI. Mainly there are four types of imagers: spatial scanning, spectral scanning, spatio-spectral scanning and snapshot(49).

A spatial scanner, also called a point scanner, records the spectrum of a spatial point which results in 1D spectral information. These spatial scans will be repeated several times so multiple points can form a 2D area, a so called whiskbroom imager. Data acquisition may take a substantial amount of time, due to the facts that each point needs to be scanned repeatedly. A faster alternative is a line-scanner, a pushbroom imager. By using this method it is possible to

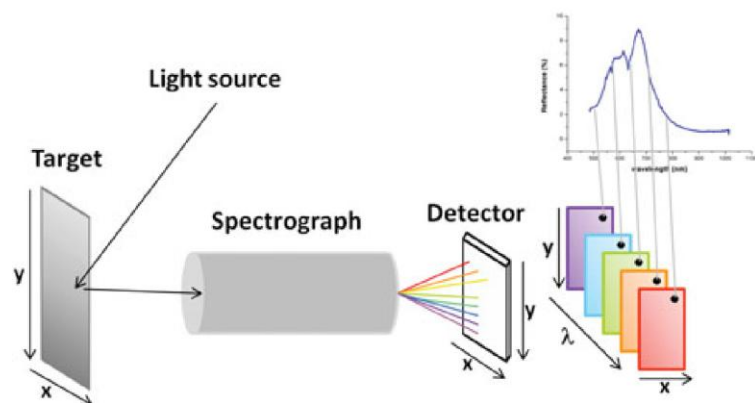


**Figure 2 Working mechanism HSI**

capture an individual spectrum for each point on a line in the spectrum. The pushbroom imager scans in the orthogonal direction of the datacube. The spatio-spectral imager has the same principle as the pushbroom imager, only this one scans a diagonal slice from the datacube. This requires motion between the detector and the sample for building the datacube. A snapshot imager obtains all the information required to build a datacube in one scan. Out of these four imagers, the pushbroom imager has the highest spectral resolution from a broad spectrum line. Its need for motion however increases its data acquisition time (47).

HSI generates a 3D dataset obtained from 2D images based on spectral and spatial information. Spectral information enables HSI to identify pathological structures and spatial information can

identify the source of each spectrum. This dataset is known as a hypercube. The image shows the hypercube(50). The hyperspectral camera can obtain 346 spectral bands between 400 and 1000 nm. These bands are acquired with intervals of 1.73 nm per second which results in an image of 400\*600 pixels(51). The penetration depth of the light depends on the absorption inside the tissue, mostly light between 600 and 1300 nm is absorbed. Variation in the refractive index of tissue components results in scattering. In cells these variations are caused by organelles. These organelles are specific for each type of tissue which is why obtained spectra can give information about tissue properties(52).

An overview of available HSI systems and their applications is given in *table 5* (48).

Hyperspectral imaging systems used in medical applications

Name	Manufacturer	Number of bands	Spectral range (nm)	Spectral resolution (nm)	Medical applications
CRI Maestro Systems	Caliper, Hopkinton, MA	100	450-950	5	Cancer detection
ImSpector Spectral Camera	Spectral Imaging Ltd., Oulu, Finland	238	1000-2500	6.29	Cancer detection
HSCI 700 Hyperspectral Camera	Hokkaido Satellite Corp., Hokkaido, Japan	72	400-800	5.6	Cancer detection
HyperMed CombiVu-R System	HyperMed, Inc., Waltham, MA	20	500-600	5	Tissue oxygenation assessment
OxyVu	HyperMed, Inc., Burlington, MA	15	500-660	10.6	Tissue oxygenation assessment
HyperMed, Visible MHSI System	HyperMed, Inc., Watertown, MA	30	—	—	Tissue oxygenation assessment
HySpec	Norsk Elektro Optikk AS, Lorenskog, Norway	160	400-1000	3.75	Tissue oxygenation assessment

**Table 5** Hyperspectral imaging systems

There are different ways to apply HSI, this will be summarized below.

#### *Fourier transformation infrared imaging HSI (FTIR-HSI)*

Fourier transform infrared imaging (FTIR) combines a Fourier transformation spectrometer and a focal plane array. The focal plane array collects spectral and spatial information in different directions(53). FTIR collects images as a function of interferometer optical path differences. The next step is translating these spectral images to the frequency domain to form the final hyperspectral cube. This way every spatial location of FTIR data in the imaging plane is recorded. Mid-wavelength infrared spectroscopes in medical applications are all FTIR(54).

Serial acquisition systems can only collect a fraction of the full hypercube. Using FTIR it is possible to collect the full hypercube with increased speed, and better image size, resolution and signal-to-noise ratio(54).

During the study of Thiago et al. on thyroid tissue with FTIR spectroscopy they have been able to interpret HSI data and protein conformational changes. The data was imported in MATLAB software, which was able to interpret the data and show differences between samples. The data was normalized, noise filtered, corrected for influences of water-vapour and scattering effects. This study shows promising results in tissue research using FTIR spectroscopy and might contribute to the design of our research experiment (55).

FTIR is commonly used for examining fixed tissue sections during pathological examination. These examinations can be performed in two ways. Tissue properties can be obtained from transflected light and transmitted light (*see figure 3*). Although the transflection mode results in more artefacts, it is commonly used because of its cost-effectiveness. In Perez-Guaita et al. the influences of the transflection mode were examined. So even though more artefacts occur using the transflection mode, the results are comparable with the transmission mode after a standard pre-processing. This overall conclusion is based on a lymphoma and should be reconsidered for each setting. Most differences between the modes are derived from the electric field standing wave (56).

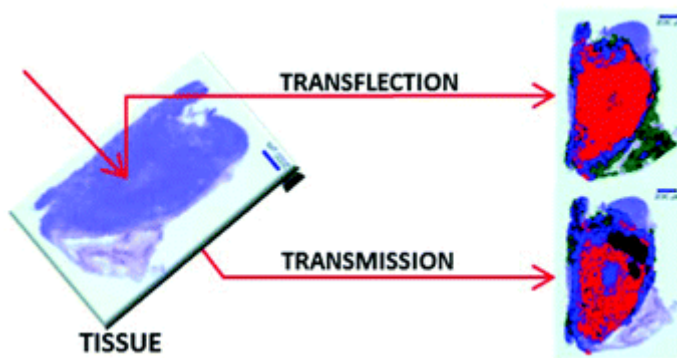


Figure 3 principle of transmission and transfection

#### Video camera HSI

It is possible to combine the pushbroom imager with a video camera. This results in different advantages such as: easier interpretation due to colour imaging, samples of different thickness can maintain the same working space, easier positioning with small field of view and repeated scanning can be prevented. With the video camera the region of interest can be selected so unwanted scanning is prevented and acquisition time is decreased. This solves the disadvantages of pushbroom imaging and a high spectral resolution is acquired at a small data acquisition time (47). This combination improves the requirement of a good field of view.

#### Multimodal confocal hyperspectral imaging microscopy

Conventional microscopy uses a CCD-based spectrometer (57).

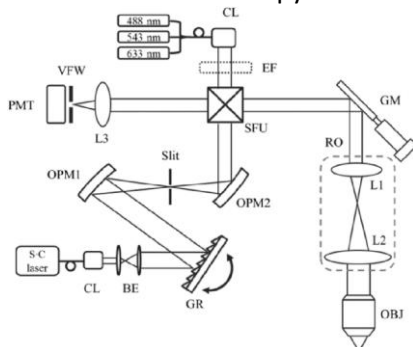


Figure 4 multimodal confocal hyperspectral imaging microscope

Multimodal confocal hyperspectral imaging microscopy is a new proposed system using a photomultiplier tube as detector for microscopy. The system is simple, robust and fast due to a monochromatic light source designed for hyperspectral imaging. Figure 4 shows the design of the new microscope with a spectral resolution of 5 nm. This technique obtains structural and chemical properties and is useful without labelling, which is important in our application. According to Kim et al. it has also potential for making in vivo images in humans (58). If this technique is really promising for in vivo imaging, this might be integrated into the OR microscope (59).

#### Hyperspectral stimulated Raman spectroscopy (hsSRS)

Basically two types of coherent Raman spectroscopy are distinguished, coherent anti-stokes Raman scattering (CARS) and stimulated Raman scattering (SRS). Where the latter is most reliable and has an easy quantification. Recently hyperspectral SRS based on spectral scanning has been demonstrated. Raman spectra at all individual pixels were reconstructed. This is achieved using different scanning mechanisms and lasers, and by tuning the Raman shift. The study of Fu et al. has demonstrated the use of hyperspectral Raman data for distinguishing different subcellular components. High wave

numbers in C-H stretching regions were shown to be useful. This method can detect multiple biochemical changes and can be integrated during microscopy. The label-free nature allows in vivo quantification with high resolution (60). hsSRS has also been proven useful as a metabolic imaging technique to quantify lipids. It showed previously unknown changes in lipid composition. This technique could also be desirable for fingerprinting other metabolites (61). When LGGs show changes in lipids which are detected with MRI, it might also be possible to detect these during surgery using the microscope combining with an hsSRS system.

#### *4.2.1. Absolute requirements*

No contrast agent: HSI distinguishes different tissue properties based on how they scatter light. No contrast agent is needed for distinguishing healthy tissue properties from tumour tissue(54).

Real time imaging: HSI has the ability of near real-time imaging which is a requirement for the use during surgery. It already has been used during surgery and has been proven to be useful for tumour identification during surgery. (50)

No brain contact: No tissue contact is needed to obtain images, because light will be sent into the tissue from a small distance. HSI has been used this way in a laparoscopic system during cholecystectomy in a study by Zuzak et al (62).

In vivo imaging: It is possible to image tissue in vivo using HSI. This has already been done for distinguishing breast tumour tissue from normal tissue during surgery by Panasyuk et al (54) (50).

No significant tissue damage: There has been no research to evaluate the noxiousness of HSI. Although there have been several studies on HSI for medical applications, which gave promising results. Based on this information it is assumed that HSI is harmless, otherwise no further investigation to medical HSI would take place (50) (63) (54) (51, 64)

Based on this information, this technique complies with the requirements and therefore is worth further investigation.

#### 4.2.1. *Relative requirements*

High sensitivity and specificity: Measuring sensitivity and specificity on brain tumour tissue has not yet been demonstrated with HSI. A hyperspectral camera was used to detect metastatic lung cancer in vitro with a specificity of 97.7% and sensitivity of 92.6% in lung tissue. In lymph node slides they were able to detect metastatic lung tumour with a specificity of 98.3% and sensitivity of 96.2%(65). In research to cervical neoplasia they were able to detect neoplasia in vivo on humans with a specificity of 70% and sensitivity of 97%(66). This way HSI has promising results of high sensitivity and specificity. However, this should be reconsidered for each tissue and application. There is no guarantee HSI will have a high sensitivity and specificity applied on brain tissue.

Applicability in the OR: Years ago hyperspectral imaging already was introduced in the OR. It has been proven to be helpful for extending the surgeon's vision during surgery, so it is applicable in a regular operating room (63).

Implementation into the OR microscope: A HSI system has already been integrated into a confocal microscope, so it should also be integratable into the OR-microscope(59)

Field of view: In one HSI study, the spectral range is 600-1100 nm, with a mean bandwidth of 6.95 nm. These settings resulted in a 7.6 cm diameter field of view with an optimal spatial resolution of 0.24 mm. These values are right for brain tissue imaging(62).

Level of development: Medical HSI has been used for in vivo research in humans on cervical neoplasia(66) and in Hattery et al. they were able to detect tumour angiogenesis and tumour metabolism using HSI to detect Kaposi's sarcoma(67). Furthermore in Chaudhari et al. they were able to detect a human glioblastoma implemented into a mouse(68).

## 4.2.2 Optical Coherence Tomography

Optical Coherence Tomography (OCT) is often described as the optical equivalent of ultrasonography. The analogy with US becomes clear when looking at the working principle of OCT, the magnitude and echo-time delay of reflected and backscattered light is measured. This way it is possible to image the microstructure of tissues. Similar to US, an B-scan is eventually created from multiple A-scans. 3D data-sets can be created by putting A-scans in a raster pattern and is called 3D-OCT. OCT has several properties similar to microscopy as well and can be seen as an “optical biopsy” (69). The origin of OCT lies with TD-OCT (time domain OCT), this OCT method uses a Michelson interferometer (70). The first application of OCT by Huang et al in 1991, was lateral scanning of biological volume, resulting in 3D information (71).

### *Interferometry*

Interferometry is the basic principle behind OCT and will be explained. The transmitted light in an OCT system is split by a coupler into two beams: the reference beam and the sample beam. The sample beam is focussed by an objective lens on the tissue that is being examined. The reference beam is focussed on a reference mirror. This way, the reference beam propagates back to where it came from. The sample beam gets reflected by the sample. Since biological samples are inhomogeneous, light will be backscattered due to different refraction indices in the tissue. The reflected reference beam and backscattered sample beam will be combined in the coupler. This way an interference pattern will then be detected by a detector (72). *Figure 5* shows a fiber based interferometer set-up, which gives a good insight in the basic principle of OCT.

Performing interferometry on one point in the tissue sample creates a scan in the axial plane also called an A-scan. An A-scan is a one-dimensional plot containing the amplitude of the backscattered signal as a function of time. Cross-sectional images are obtained by collecting many A-scans in a line and display the amplitude of the backscattered signal in greyscale pixels. This is called longitudinal OCT or B-scanning (72). *Figure 6* shows a B-scan and the accompanying A-scans. T-scanning is another scanning method. In this case, transverse scanning is performed in one specific depth of the tissue (73). This way the same transversal plane can be imaged as a B-scan, but in less time. En-face scans or C-scans have an orientation as if the sample is watched through a microscope. C-scans can be obtained with B-scans or T-scans (74).

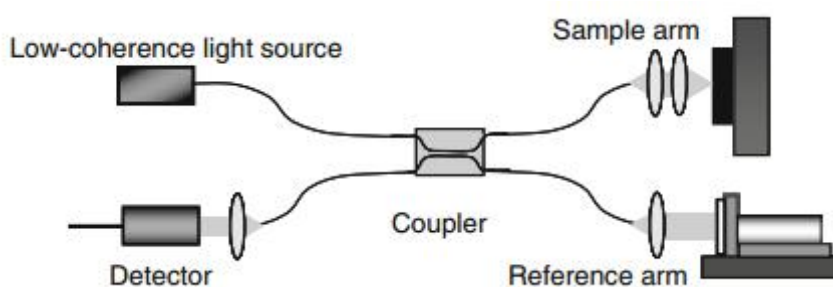


**Figure 5** A fiber based interferometer set-up. Light from a low-coherent light source is split by a coupler in a reference beam and a sample beam. Both light beams travel through different arms. The light backscattered from the reference mirror and the sample a arm are recombined in the coupler. This generates an interference pattern that is recorded by the detector.

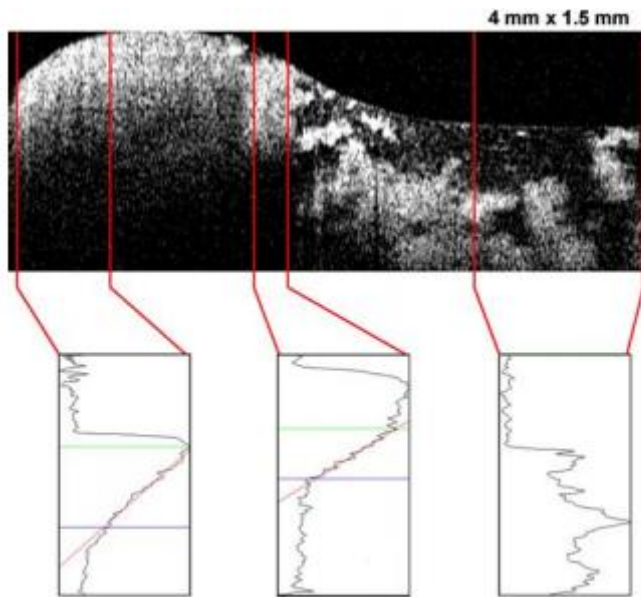


**Figure 6** B-scans (above) consists of parallel A-scans (beneath). Analyzing single A-scans, can provide depth information about the signal intensity. In homogeneous tissue, the attenuation coefficient can be calculated out of these A-scans. The B-scan presented in this figure is an HGG. The A-scans are obtained from diffusely invaded brain tissue (left), macroscopic tumour (middle) and a necrotic zone (right).

### *Resolution*

The lateral resolution can be adapted by changing the numerical aperture of the lens in the system. The lateral resolution increases with a higher numerical aperture. However, it causes the penetration depth of light to decrease (75). The depth resolution depends on the coherence length, the length in which a wave maintains the same phase relations. The shorter the coherence length, the higher the axial resolution (74). A high axial resolution can be achieved by a light source with a very broad bandwidth (76). Theoretically, axial resolution of  $2\ \mu\text{m}$  can be achieved by using a  $800\ \text{nm}$  light source with a bandwidth  $140\ \text{nm}$ . In reality this resolution is less, because light will be absorbed and scattered. Transverse resolutions of  $5\ \mu\text{m}$  can be achieved (77). In brain tissue a spatial resolution was obtained from approximately  $10\text{-}15\ \mu\text{m}$  and a penetration depth of  $2\ \text{mm}$  (78). The coherence length of the light source ought to be shorter than the difference of the travelled distance between the reference beam and sample beam, only this way interference can occur. Information about different tissue depths can be obtained by moving the reference mirror (72).

### *Fourier domain OCT (FD-OCT)*

Besides TD-OCT, FD-OCT also exists. In contrast to TD-OCT, FD-OCT does not require a moving reference mirror because light from all axial depths are detected at the same time. This way all spectral components are captured simultaneously (79). By performing an inverse-Fourier transformation the obtained data is translated to axial depth information (80). Because mechanical movements do not limit this method, it has a higher imaging speed compared to TD-OCT. For this reason, popularity for this method has increased over years. However, more data acquisition complexity and a decreased signal from zero have not been taken into account here (81). FD-OCT can also be classified in spectral domain OCT (SD-OCT) and swept source OCT (SS-OCT). SD-OCT uses a broadband light source and a spectrometer with a line scan camera. One of the greater advancements of SD-OCT is that it is able to let the source and sample beam travel through the same fibre. This is also known as common path OCT(82, 83)Therefore SD-OCT is favourable in applications where a flexible point of view is desired (72). SS-OCT uses a swept laser instead of a low coherence laser and a line scan camera instead of a photo detector (84).The choice between using SD-OCT or SS-OCT depends on which wavelength range is used. For  $1\ \mu\text{m}$  scale SD-OCT is most

favourable where SS-OCT works best above 1.3 micrometre. Recently, swept-source/ FD-OCT (SS/FD-OCT) has attracted great attention, due to its large imaging depth and speed (85, 86).

#### *Full-field OCT*

With full field OCT (FF-OCT) all pixels in a transversal section are lit simultaneously. The acquired information is comparable to T-scans. The advantage of FF-OCT is it can use incoherent spatial optical sources, this means the light source does not have to comply to high requirements and can be chosen cheaply. The disadvantage of FF-OCT is the interference amplitude is gained using phase stepping algorithms. This means it takes some time to add up all the wavelengths, resulting in non-real-time images. Another disadvantage is the limited dynamic range of the analogue to digital converter in CCD cameras, which makes FF-OCT less sensitive (74).

#### *4.2.2. Absolute requirements*

Real time: Initially real-time OCT was only possible in TD-OCT derived systems (74). There has been development in real-time imaging with FD- OCT derived systems, like SS/FD-OCT and full-field OCT. As mentioned before, SS/FD-OCT has attracted great attention in the past years due to its large imaging depth and speed. Furthermore SS-OCT was able to create in vivo, real-time 3D images of meibomian glands and FF-OCT could image rat brains in vivo, real-time (85, 87, 88). Typically a sweep rate of 100 kHz is required for real-time 3D OCT imaging. A sweep rate of up to 250 kHz has been demonstrated using a dispersing tuned fibre laser, which is developed for SS-OCT (89).

No brain-contact: OCT was already described as a possible application in neurosurgery in 1998 by Boppart et al. For imaging intracortical melanomas(90), since it is a noncontact imaging tool. All OCT types are able to imagine in a contactless and non-invasive way (75). Working distance in Finke et al. was 220 to 290 mm (91) and in Just et al. they worked with a working distances of 224 till 280 mm (92). This way there can be concluded that no brain contact is required in OCT. However the working distance creates an speckle noise.

In vivo: Since its first demonstration by Huang et al. (71), human retina in vitro scans have been made. In 1993 the first in vivo image of an human retina was made by Izatt et a (93). Furthermore, as mentioned, intraoperative real-time FD-OCT provided images in vivo from rat brains. Underlying tumour boundaries were found using OCT during this experiment and provided the surgeon with an extensive view of the surgical region (94). Moreover OCT was developed because there was a need for a real-time, high resolution in situ imaging technique, without the need for taking samples of the tissue (80). This way it can be concluded that OCT is an ideal tool for in vivo imaging.

No-contrast agent: There is existing research in the domain of the use of contrast agents in combination with OCT. One example is the use of gold nano-particles to enhance the contrast of photo-thermal OCT, which is a tool for molecular imaging (95). Another example is polypyrrole nanoparticles, which are considered to enhance the contrast of OCT imaging for detecting tumour cells (96). Nevertheless, since OCT measurements are based on the magnitude and echo-time delay of backscattered tissue a chemical contrast agent is not required for OCT (72).

No tissue-damage: One of the main advantages in OCT compared to other imaging systems is it does not require harmful radiation (97). The most used light sources operate in the near infrared (NIR) light range. Super luminescent diodes (SLD), which operate around 800 nm are used more often(97). Due to the use of NIR, there is a minor radiation exposure compared to other tomographic techniques (72). Furthermore, all OCT types make images in a contactless and non-invasive way (75).

#### 4.2.2. *Relative requirements*

Sensitivity and Specificity: Bohringer et al. researched detecting residual tumour cells in the resection areas. Both TD-OCT and SD-OCT could detect HGGs and allowed both 1-1.5 mm imaging depths. The used samples were obtained from human brain biopsies and the distinction was based on differences in attenuation coefficients between tumour tissue and healthy tissue. The attenuation coefficient presented differences in microstructures (78). Another blinded clinical pilot study researched microsurgical human GBM resections with OCT based on the attenuation coefficient. The samples were histologically evaluated, 15 biopsies contained diffuse tumour infiltration and 12 were healthy tissue. From these tumour samples 9 were scored as “abnormal microstructure” and from the healthy tissue samples also 9 were scored as “normal microstructure”. This leads to a sensitivity of 60% and specificity of 75% (98). Furthermore in Assayag et al, WHO grade II glioma samples were compared to histological coupes. They concluded diffuse low-grade gliomas are mistaken for normal brain tissue too often, because the tumorous cells are too dispersed through the normal brain tissue. Hence, histological architectural changes are only detectable when the diffuse glial cell density is greater than 20% (99). Using distinction based on architectural changes, en- face OCT scans were able to image high-grade glioma, but this was not reliable for low-grade gliomas (99).

Field of View: C-scan based OCT like FF-OCT can achieve a native field of view of 1 mm<sup>2</sup> (100). However it is possible to stitch multiple fields together for obtaining a high-resolution image with a FOV of 1 cm<sup>2</sup>, the resolution is 10-15 μm (101). A FF-scan of 2.25 cm<sup>2</sup> is performed in 7 min (102).

Applicability in OR: The working distance of the research described above was 220 to 290 mm (91), which is suitable for use in the OR. OCT has also been used in the OR for brain surgery (91). Furthermore, OCT is usually integrated into a microscope, which makes it a mobile imaging device. This way it is applicable in the OR (92). Furthermore, several studies have tested the feasibility of OCT in an operating microscope, for retinal surgery. Binder et al concluded that intraoperative OCT can improve the amount of information that can be obtained in retinal surgery. However, they also described that the system was rather complex, so the aid of an assistant was needed (103). Ehler et al did research into the possibility of dynamic imaging of surgical motions with a microscope-mounted SDOCT. They concluded that motion capture with this technique was not satisfying. Motion capture in 3D was not possible in real-time. Also in this research, aid of an assistant was required, because of the lack of a tracking system (104). A feature which may increase the ease of use of OCT during surgery is a head-up display. Ehlers et al. demonstrated a intraoperative OCT integrated with a HUD system (105).

Implementation into the OR Microscope: The required working distance of OCT and the acquisition rate of the A-scans allows the implementation of OCT in the operating microscopes (106). Major advances have been made in the development of microscope integrated optical coherence tomography (MIOCT). All of these intraoperative OCTs are developed for ophthalmic surgery. The nomenclature changed from microscope-mounted (MMOCT) to MIOCT, because OCT became increasingly integrated with the operating microscope (107). SD-OCT is the preferred OCT technique used in MMOCT, due to its faster data acquisition time, larger field of view and higher resolution (108).

Level of development: Kantelhardt et al. developed a prototype of a robotized OCT-integrated operating microscope. Large surface areas could be automatically scanned, so OCT has already been applied for tumour resection in humans (109). The article stated that in the future, operating microscopes may be used in neurosurgery, to acquire data of brain tumours. Klein et al. designed a swept source laser which reached 1,368,700 axial scans per second, which is 50x faster than

commercial instruments. The high speed of the system made it possible to obtain 1900x1900 A-scans in 3 seconds with a 70 degrees angle of view (110). Extremely fast tuneable broad bandwidth light band sources enable OCT to achieve very high detailed images. For example Ti: Sapphire lasers are excellent light sources for UHR OCT, since these have a very broad bandwidth (approximately 300nm)(77). OCT has been applied in human tumour resection in neurosurgery on grade III and IV glioma and could differentiate between areas of tumour and healthy tissue (106). Unfortunately, it is currently not suitable for imaging LGGs yet (99).

### 4.2.3 Optical coherence elastography

Optical coherence elastography (OCE) is based on the mechanical deformation of tissue and its resulting tissue displacement, which is imaged with OCT. With this displacement, a mechanical property or parameter is calculated to create an elastogram which represents the stiffness of the tissue (111). The first step in OCE is mechanically loading the tissue. Different loading methods can be divided in three major categories based on the manner of deformation.

The first category is compression OCE, an external load is applied to the whole tissue region which is imaged (*see figure 7*). The strain is calculated from the changes in displacement. Stress can be determined from the applied loading force in relation to the cross-sectional area. Stiffness is the ratio between the stress and strain (112). For this calculation, an assumption has to be made that the applied stress over the area of interest is uniform and the tissue is isotropic homogenous. *Figure 7* Schematic (left) and photograph of load transducer for in vivo optical coherence elastography of human skin. This is not the case in brain tissue, so the stress is unknown throughout the sample. As a consequence, this method only gives a qualitative measurement of the stiffness of the entire tissue sample, also imaging artefacts will appear in the resulting elastogram. Despite this major limitation, the spatial resolution is still equal or nearly equal to OCT structural imaging (113).

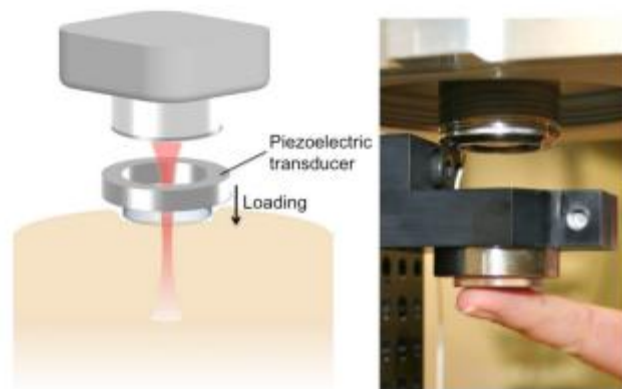


**Figure 7 Schematic (left) and photograph of load transducer for in vivo optical coherence elastography of human skin.**

The second category is shear wave OCE which involves the characterization of elastic wave propagation in the tissue. Displacement propagates as mechanical waves within the tissue. Under ideal circumstances and a known tissue density, tissue stiffness can be directly quantified from the phase velocity of the propagating wave (114). Both shear waves and surface waves can be used to quantify stiffness. Shear waves propagate in the bulk of a material and surface waves on the surface of a material (115).

The third category, resonant OCE, is based on the assessment of the natural frequency of the tissue. The employment of the natural frequency as an indicator has a direct and an indirect form. The direct form is based on the fact that the square of natural frequency appears to be linearly related to the stiffness of the sample (116). Therefore difference in stiffness in a sample means difference in natural frequency, which can be used as a direct mechanical contrast. An indirect mechanical contrast can be measured by detection of displacement- or strain related parameters while applying the loading frequency. Amplitude or strain increases when the external driving frequency matches the natural frequency of the tissue. Difference in stiffness within a tissue causes different natural frequencies, so spatial mapping of the vibrational spectrum can be used to make an elastogram (117).

When the tissue is loaded in one of the previously described ways, accurate and sensitive measurement of tissue displacement is the next step. Most OCE techniques use speckle tracking or phase-sensitive motion for this purpose (118). Backscatter in OCT images of dense tissue is detected as speckles. Speckle tracking is a technique to track the speckle motion between successive OCT frames. Changes in speckle pattern are detected when the tissue is mechanically loaded (111). Phase-sensitive motion uses phase changes between successive scans to determine tissue displacements in real-time. This provides a significant improvement in the elastogram quality due to its higher sensitivity (119).

#### 4.2.3. *Absolute requirements*

Real-time: OCE measurements of the cornea can be conducted in real time due to Fourier domain OCT (120-122). This is a wave-based, noncontact technique which does not seem suitable for brain tissue (see requirement noncontact). On the other hand, compression OCE has more potential for real time imaging of brain tumours and has a rapid scanning speed of five seconds (118).

In vivo imaging: In vivo imaging generally requires stimulation and imaging of the tissue to be on the same site. In vivo imaging of soft tissue is possible, but in recent studies tissue contact was required. A 3D-OCE system was applied to normal and hydrated skin. A ring actuator compressed the tissue to provide mechanical stimulation (123). The needle OCE technique is another contact method which holds great promise for intraoperative tumour imaging. OCE was integrated in a needle probe to detect tumour margins in situ in excised human breast tissue. The flat needle tip compressed the tissue. Based on its mechanical properties, the tumour could be distinguished from the adipose tissue (124). One of the early efforts to a non-contact in vivo method was an air puff system which deformed the cornea using an air stream. This technique provides images of the human corneal dynamics (125).

No brain contact: Surface acoustic waves (SAWs) have been generated in order to create noncontact OCE methods. Noncontact methods include an air stream (125) and thermo-elastic expansion induced by light absorption(122). SAW-OCE is only suited for homogeneous tissues like the cornea, since heterogeneous tissues (soft tissue for example) cause a large degree of mechanical heterogeneity. This heterogeneity causes a lower resolution, and therefore SAW-OCE is not suitable for imaging soft tissue tumours. Compression OCE seems more suitable for heterogeneous tissues like gliomas due to the higher spatial resolution, but this requires tissue contact (118).

No significant tissue damage: OCE is a non-destructive technique. Loading the tissue causes a sub-micrometre deformation which is low enough for the tissue to maintain its structural and functional properties(126). OCT images tissue displacement with non-ionized radiation, which does not damage tissue either(74).

No contrast agent: OCE uses the different elastic properties of tissue as a contrast mechanism to form images without the use of a contrast agent (111). With ultrasound shear wave elastography (US-elastography), it was determined that LGG is stiffer than healthy brain tissue (32). OCE is based on the same principle as US-elastography, which would imply the same contrast differences between LGG and healthy brain tissue.

### 4.2.3. *Relative requirements*

Sensitivity and specificity: OCE has not yet been applied to brain tissue. Further studies are required to establish the possibility of OCE to distinguish LGG from healthy brain tissue and its sensitivity and specificity. OCE has great potential of reliable detection of tumour margin. The resolution of OCE reaches microscopic level with a spatial resolution in the micrometre range. This provides the possibility of highly detailed examination of the tissue and visualizes micro-scale heterogeneity within tissue. OCE enables high signal-to-noise ratio (SNR) detection of nanometre tissue deformation (126). OCE was able to detect malignant breast tumours, which is a soft tissue tumour like gliomas(124). In an article by Kennedy et al. compression OCE is tested on tissue phantoms with different properties and it was possible to contrast features with a elasticity's modulus ratio of just 1.1:1. Furthermore this research predicts that a theoretical elasticity's modulus ratio of 1.002:1 is possible. Based on these results there can be concluded that OCE is a highly sensitive imaging device. However to achieve this high sensitivity also a high OCT SNR is required, which is hard to achieve in soft tissues and highly scattering tissues (113). The sensitivity and specificity of a OCE system are fundamentally limited by the phase sensitivity of the OCE SNR of the system (127). Besides, Ultrasound Shear Wave Elastography measured a significant difference between the stiffness of LGG and healthy brain tissue. Since OCE provides contrast based on the same principle, OCE seems promising for the application on LGG (32).

Field of view: OCE has the same or a larger field of view compared to OCT. the FOV is 0,01 cm to 1 cm and the spatial resolution is 0.01 mm to 0.1 mm (126). Such a resolution provides detailed information on a microscopic level, with the potential to image heterogeneity in LGGs and healthy brain tissue. The penetration depth is only millimetres into tissue, but is not a limitation for the distinction of malignant tissue(128).

Level of development: Over the past five years OCE has undergone a rapid technological development. Multiple forms of OCE have been successfully applied on different types of tissues. It has been used for noncontact measurement of the cornea and are a first step in the assessment of its mechanical properties. Photo thermal and air-puff are two promising loading mechanisms for this application (125, 129). In an ex vivo rabbit artery wall, OCE could detect atherosclerotic lesion and fibrous caps (130). OCE technique is also used to image and measure the elasticity of skeletal muscle (131) and cardiac muscle (132). OCE can differentiate between necrotic lesions from intact skeletal muscle tissue and tendons in ex vivo mouse samples. In ex vivo mouse cardiac muscle, OCE can distinguish normal and genetically altered myocardiocytes (132). Three-dimensional optical coherence elastography was able to monitor hydration of the skin in vivo (123). SAW elastography can detect a hard nodule in forearm skin in vivo (133). OCE has not been applied yet in gliomas, although it has been used in other soft tissue tumours. In ex vivo mammary rat tissue spectroscopic contrast was observed between adipose tissue and tumour (117, 134). On excised human breast tissue, needle OCT visualised tumour margins (135). Before OCE can be implemented in an intra-operative setting, it has a long way of development to go. Besides this fact, it has not been used on gliomas yet, so it is uncertain if it can make a contrast at all.

Applicability in the OR: Based on the level of development, only an estimation of applicability in the OR can be made. The current OCE techniques have not been applied yet in a preclinical or clinical settings yet (126). Based on the level of development, it is difficult to estimate the applicability in the OR. The current OCE techniques are not advanced enough yet to be applied in clinical settings. Efforts for development have been made to make OCE applicable in the OR (120). In 2012 Shang Wang et al. developed an OCE system for noncontact elasticity measurement of tumours in soft tissue. They used an air-puff system to bring displacement into the tissue. They concluded that this

method has potential to be applied in the OR, with further investigation(136). Since OCE is an extension of OCT(137), one would expect OCE will face the same advantages and complications as OCT applied in the OR. The extension of OCE compared to OCT would be an air-puff system or a mechanical system (however, a mechanical system will cause brain contact) that brings a mechanical load into the tissue. It is not known to what degree the process of bringing this load interrupts the surgical procedures.

Implementation into the OR microscope: OCE is elastography combined with OCT. OCT can be integrated with an intraoperative microscope for retinal surgery (107). However, OCE was only integrated into a needle probe (124). In OCE a mechanical stimulus has to be applied to deform tissue and in certain OCE methods this involves tissue contact, which complicates integration into a microscope.

#### 4.2.4 Infrared spectroscopy

IR spectro-imaging is based on the unique vibrational transitions in covalent bonds as a result of absorption of IR radiation (138). For near-infrared (NIR), the absorption of electromagnetic energy is 14000-4000  $\text{cm}^{-1}$  and 4000-400  $\text{cm}^{-1}$  for mid-infrared (139). The IR spectrum shows characteristic peaks which reflect the contribution of proteins, lipids, carbohydrates and nucleic acids, plus a great variety molecules that occurs in cells in low concentration (140). The obtained spectral patterns are correlated with the specific properties of a cell (141). IR spectra of glioma cells contain an important source of information about the origin of a cell and its characteristic behaviour in vitro as well as in vivo (142). IR spectro-imaging has been used for analysis of normal and pathological brain tissue samples for years (143, 144). The IR spectra for normal brain tissue and brain tumours overlap largely in the biochemical region (1800  $\text{cm}^{-1}$  to 900  $\text{cm}^{-1}$ ). Although some significant differences can be distinguished in de the region of 1050–1000  $\text{cm}^{-1}$  (carbohydrates and collagen), 1300  $\text{cm}^{-1}$  to 1150  $\text{cm}^{-1}$  (Amide III and PO<sub>2</sub><sup>-</sup>) and 1760  $\text{cm}^{-1}$  to 1700  $\text{cm}^{-1}$  (lipids, DNA/RNA and Amide I). The wavenumbers separating low-grade astrocytoma from normal brain tissue are 1103  $\text{cm}^{-1}$ , 1234  $\text{cm}^{-1}$  (nasPO<sub>2</sub><sup>-</sup>), 1470  $\text{cm}^{-1}$  (lipids), 1504  $\text{cm}^{-1}$  (Amide II) and 1628/1686  $\text{cm}^{-1}$  (Amide I). These specific wavenumbers allows the identification of molecular markers that can be utilized to distinguish LGG from healthy brain tissue (145). Furthermore IR has been able to distinguish malignant and benign tumours in breast, colon, lung and prostate tissues (146). IR-spectroscopy has three major modes to image samples: transmission, transfection and attenuated total reflection (figure, below) (147). Each mode offers convenience for some samples and challenges for others. In transfection mode the sample is placed on an IR-reflecting surface and measurements are generated by a beam passing through the sample and reflecting back from the substrate through the sample (146). Although transfection mode results in more artefacts, it is commonly used because of its cost-effectiveness. In Perez-Guaita et al. the influences of the transfection mode are examined. Even though more artefacts occur, after a standard pre-processing the results are comparable with the transmission mode. However, this is an overall conclusion based on a lymphoma and should be reconsidered in each setting. Most differences between the modes are derived from the electric fields standing wave (148). In ATR-FTIR mode the IR beam passes through an internal reflection element with a high refractive index (see *figure8*). A disadvantage of this mode is that the sample must usually be in direct contact with the internal reflection element (149). Moreover, it was able to distinguish brain tumour from healthy brain tissue by the distribution of glucose and lactic acid in tumours (150).

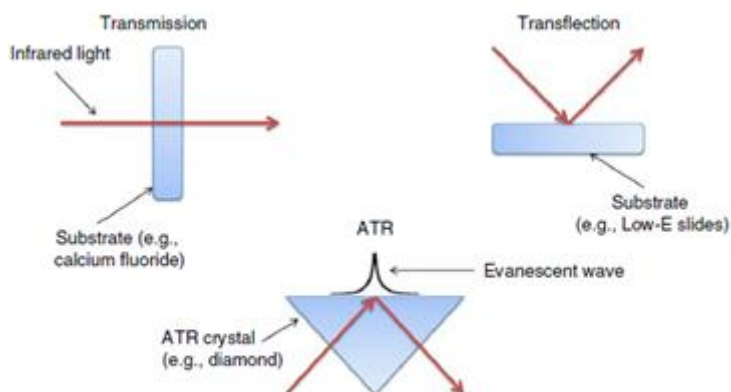


Figure 8 Using Fourier transform IR spectroscopy to analyse biological materials Matthew J Baker<sup>1,13</sup>, Júlio Trevisan

#### TIR-PDT Spectroscopy

A new IR-spectroscopy technique is TIR-PDT spectroscopy, which is developed to measure glucose concentration in vivo. It is based on the following principle. After the absorption of IR light by a

sample, the radiation less de-excitation of the vibrational-rotational states produces a temperature increase of the irradiated spot. If the produced heat diffuses to a material in contact with the sample, a temperature gradient in a thermal lens is generated in the coupled material (151).

#### 4.2.4. *Absolute requirements*

No brain contact: Samples of dopamine solution were measured in a "noncontact mode" using scanning force microscopy with ATR-FTIR. This proves IR images can be made without making contact (152).

In vivo imaging: Infrared spectroscopy is originally an in vitro technique. Also ATR-FTIR can only be used on ex vivo samples, because water influences the spectra and a dry tissue sample is required (153). However, IR spectroscopy in combination with a tuneable laser source and a small fibre-optic attenuated total reflection (ATR) sensor is an promising in vivo method (154). AFR-FTIR imaging also allows analysis of live cells in aqueous systems (155).

Real time imaging: A Fourier transform infrared spectrum of all cell constituents is recorded on the intact cells within a few minutes (156). Fourier-transform IR also has the ability of wide-field scanning of a sample in seconds, providing tens of thousands of spectra (146). ATR-FTIR images intact cells in a few seconds and tissue sections in a few minutes (145).

No significant tissue damage: FT-IR can be used to analyse tissue damage caused by physical force in a way that does not damage the tissue(143). Photo-acoustic FTIR was performed on an undisturbed human cortical bone. This technique can detect absorbance spectra from unprepared samples at controllable sampling depth. It is a non-destructive technique(157).

#### *No contrast agent*

FR-IR spectro-imaging does not require the addition of an external contrast agent(138).

#### 4.2.4. *Relative requirements*

High sensitivity and specificity: There are some general factors that may complicate the interpretation of infrared spectra. These are overtone and combination bands, Fermi resonance and coupling. Overtone bands are multiples of the fundamental absorption frequency. The first overtone appears in the spectrum at twice the wavenumber of the fundamental. When two fundamental bands absorb energy simultaneously, a combination band appears. Overtones and combination bands can have the same frequency as a fundamental band. This leads to two bands appearing close together. These two bands are called a Fermi doublet and this effect is called Fermi resonance. Coupling occurs when vibrations in the skeletons are not restricted to one or two bonds, but may involve a large part of carbon backbone and oxygen or nitrogen. As a result the energy levels mix and bands can no longer be assigned to one bond. Each wavenumber is more or less correlated with its neighbours. An infrared spectrum shows about 1100 variables, but these variables are not independent. They are composed out of peaks of different widths, which are representative for the types of molecules present in the cells (142). With computational algorithms like principal component analysis (PCA), linear discriminant analysis (LDA) and fuzzy cluster analysis, potentially relevant spectral markers can be identified and classification can be facilitated(158). In a study of brain tissue with secondary brain tumours, healthy brain tissue could be identified with a specificity of 98,7% and a sensitivity of 98.8%. Secondary brain metastases were detected with a specificity of 94,5% (153). IR spectroscopic imaging was able to distinguish LGG samples from HGG samples. All of the 22 high-grade tumour samples and 31 out of the 32 low-grade tumour samples were consistently categorized as high-grade and low-grade tumour tissue. This results in an improved sensitivity of

100% and a specificity of 96.6%. (159). Furthermore, in a study of classification of malignant gliomas, spectra of grade II astrocytoma and normal brain tissue could be distinguished in 5 samples. Bands of lipids (1,085, 1,240, 1,467, 1,740, 2,851, 2,922  $\text{cm}^{-1}$ ) and cholesterol (1,382  $\text{cm}^{-1}$ ) in IR spectra of astrocytoma grade II are lower than IR spectra of normal brain tissue. The lipid to protein ratio is 0.26 for astrocytoma grade II and 0.50 for normal brain tissue (160).

Applicability OR: FT-IR is considered to be a very promising technique when it comes to real time intraoperative diagnosing of cancers, and to improve the visibility of the margins (161). This shows IR spectroscopy is considered to be applicable in the OR in the future. Nevertheless, IR has never been applied in the OR yet. The main limitation is it is not yet possible to combine noncontact measurements with real-time imaging. Nowadays a probe is required for real-time imaging. This leads also to interruption of the surgical procedure.

Implementation into the OR-microscope: A spectrometer can be combined with an optical microscope. A microscope spectrophotometer is an additional component for a stand microscope, while a micro spectrophotometer is a fully integrated instrument (162). This suggests that a spectrometer can also be integrated into an OR-microscope.

Field of view: IR-spectra were obtained using 250 x 250  $\mu\text{m}$  sampling area to discriminate between normal brain tissue and different types of brain tumours (145). In a study by Bergner et al. an FOV of 350 x 350  $\mu\text{m}$  was acquired (153). The penetration depth of TIR-PTD in skin is around 2–4 mm in skin, depending on the wavelength of the excitation beam and the refractive index of the IRE (151). FTIR has a sample aperture of 10-20  $\mu\text{m}$  which acquires a single cell and large organelle lateral spatial resolution(147).

Level of development: FTIR spectroscopy can differentiate between primary glioblastoma and normal tissue based on their molecular properties (150), FTIR could become an important diagnostic tool to diagnose brain cancer ex vivo and in vivo, but no FTIR systems are available yet for use in the OR. For example in the OR, easy to use systems have yet to be developed (163). The technique with the lowest level of development is IR-spectroscopy. FTIR could distinguish glioblastoma from healthy brain tissue in human cells in vitro (149), but it has not been applied yet on brain tissue in vivo yet (150).

#### 4.2.5 Nonlinear microscopy

Nonlinear microscopy principles are based on auto fluorescence and uses the absorption of photons in cells to show the contrast (164) (165). Photons will be delivered by a focused photon excitation laser beam which is also a laser scanning microscope. In laser scanning microscopy the sample is scanned point by point (166). This laser beam is the same in the different variants, so they can be combined mutually to improve the images. At the point of focus from the laser the photons have a well-defined wavelength and occur in high densities. Outside the point of focus the photon density decreases rapidly (164) (165).

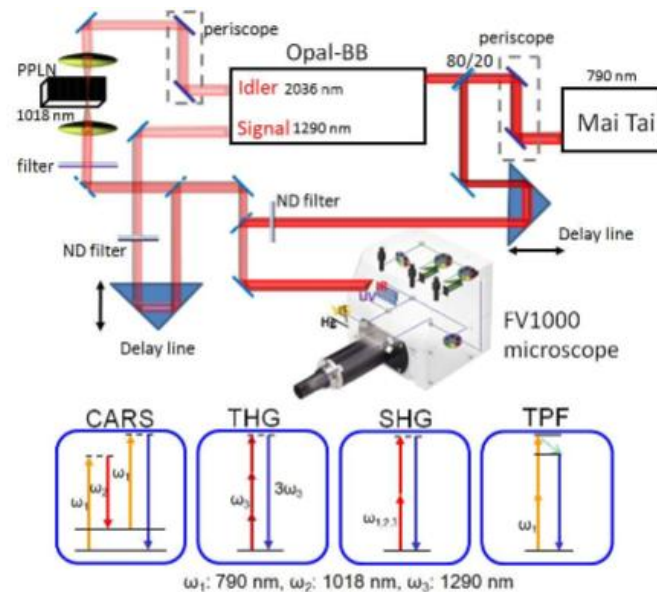


Figure 9 working mechanism of nonlinear microscopy

Two subcategories of nonlinear optical microscopies are higher harmonic generation microscopy and photon excited microscopy. Higher harmonic generation microscopy include coherent anti-stokes Raman spectroscopy (CARS), second harmonic generation microscopy (SHG) and third harmonic generation microscopy (THG). Photon excited microscopy include two-photon excited fluorescence microscopy (TPF) and multi-photon excited fluorescence microscopy (MPEF).

These techniques are powerful tools for high-resolution, high-contrast and three-dimensional imaging of living cells and tissue structures (167) (164). Due to its ability to image entire networks of cells in living organisms and its increased depth penetration compared to confocal microscopy, nonlinear microscopy has become an important tool in neurology. The most well-known type is TPF and almost all of the other variants are based on TPF (168). *Figure 9* shows a schematic diagram of nonlinear microscopy (169).

Photon excitation can be achieved with two or multiple photons interacting at the same time with the same cell. This interaction consists of photon absorption in the case of TPEF. Using multiple photons and thus multiple excitation beams gives many advantages. Among others multiple excitation beams give faster scanning time results. Furthermore a lower energy level is required to interact which reduces photo bleaching. For instance using two photon excited microscopy, half of the energy is required compared to single photon excited microscopy. Moreover multiple excitation beams use longer wavelengths which results in deeper penetration depth, less photo damage, less background and less diffraction. However, a higher order of nonlinearity is reached which produces weaker signals (164). The difference between multiphoton excited microscopy and multi harmonic generation is that in multi harmonic generation microscopy the photons will scatter due to the

process of harmonic up-conversion (170). In the case of multi harmonic generation microscopy two photons in SHG or three photons in THG are used for interaction with one cell at the same time, SHG and THG respectively. The contrast obtained with second and third order nonlinear light-matter interactions are induced with a high numerical aperture at the focus point of its objective. The scattered light is detected on a detector to form an image (166). SHG uses pulsed lasers within the near infrared spectrum, which is less phototoxic because it scatters less. Although high laser intensities are used, this wavelength range does not lead to photo bleaching, photo damage or heating effects. This is because SHG only uses virtual energy transitions, without real electron transitions. Avoiding the risks caused by these transitions and improving fast and sensitive detection (165, 171) The disadvantages of SHG imaging are that the signal intensities are weaker than those of TPEF and the scattering pattern is not optimal for good detection. Furthermore SHG has little penetration depth in size of tenth to hundreds micrometres, depending of the density of organs. The higher the tissue density, the lower the penetration depth can be achieved due to scattering in the tissue (171) (172). THG provides 3D resolution and has better penetration depth (173). Second harmonic generation microscopy (SHG) requires asymmetrical radiation sources and images based on surface properties. The emission pattern is determined to be in two lobes in case of asymmetric sources (170). Third-harmonic generation (THG) microscopy uses both symmetric or asymmetric radiation sources which makes THG sensitive for interfaces and heterogeneities (164). In symmetric sources the emission pattern is determined to be a cone, so in THG the emission pattern is in two lobes as well as in a cone. This is the reason why THG signals may occur in volumes and surfaces instead of just surfaces. The image shows the lobes and cone in THG and SHG (170). Overall SHG microscopy is able to image the overall structure of tissue where THG microscopy is better in imaging the boundaries between structures (174). THG cannot detect signals when focussing on homogeneous tissue, because signals are produced due to interfaces and optical inhomogeneities are sized comparably with the size of the beam focus (173). THG is based on differences in refractive indices, which causes the scattering and forms the image. Mainly mitochondria, lipid bodies and lysosomes produces high signals in THG, resulting in unique structural and anatomical information (175). In Débarre et al. It has been proven that the contrast obtained with THG is mainly caused due to lipid bodies. Those lipid bodies can be detected with high specificity and show the lipid body metabolism in cell physiology and tissue physiology. Lipid bodies accomplish many different functions in many different cells and tissues (173). Based on the lipid bodies it is possible to visualize neurons in living brain tissue. Resulting in high-contrast, non-invasive, label-free imaging of living neuron cells. This way it can distinguish neurons, white-matter or grey-matter and blood vessels simultaneously (176).

A different type of nonlinear microscopy is CARS, which is based on the inelastic scattering of multiple photons due to different tissue properties to obtain an image (177). CARS uses very strong collinear lasers to illuminate a sample. The wavelength of the first laser is usually constant while the wavelength of the second laser can be adapted to the same frequency of a spectral inelastic scattering peak of interest to increase the signal. This results in a stronger signal than regular Raman scattering (178). CARS can detect tissue properties based on different molecular properties and so lipids in brain structures and tumours can be shown (179) (180). This may be a promising outcome for this application but it should be investigated more and there should be a bigger field of view.

#### 4.2.5. *Absolute requirements*

No brain contact: For all nonlinear microscopy techniques obtaining a signal is based on the use of near infrared light sent into tissue. The reflected signals will be collected on a detector. This principle does not require contact with the tissue. However, nowadays these techniques are not used on humans without taking biopsies. In vivo tests were done on really small animals and when looking at

the used designs the distance between sample and objective were very low, although no specific distance were given (181-183).

In vivo imaging: In Witte et al. THG images from brain tissue were already obtained from mice during in vivo investigation. They were able to show blood vessels with a depth resolution of 2-3 neuron layers, which could be improved by using higher pulse intensities (184). In vivo imaging is also possible using CARS. In a study by Evans et al. this was done in video rate on mice ears (180).

Real-time: In the same study by Witte et al. they were also able to monitor a neuronal resting membrane potential real-time with THG(184). In Wu et al. they were able to image collagen in lymphedematous skin real-time using SHG and TPEF (185). Those techniques and a semi-automatic algorithm were combined to detect prostate tumours, and with improvement of the software, this technique could be used for real time imaging (186). Overall, nonlinear microscopy devices are able to image tissue in real-time.

No tissue damage: A high density of photons leads to photo bleaching, photo damage and heating effects. Although high laser intensities are used, it does not lead to these damaging effects due to the lasers wavelength. The used near-infrared light is a less phototoxic wavelength because it causes less scattering. Since photon densities decrease rapidly in the out of focus area, photo bleaching does not occur and so photon excited microscopy will be a suitable imaging device for using in vivo. This principle also counts for SHG, THG and CARS (164).

No contrast agent: There are TPEF derived imaging techniques which require fluorescent probes to image contrast. SHG, THG and CARS however does not requires contrast agent. Their contrast is based on discontinuities in the focus point of the laser beam, which shows the structures of cells. (181)

#### 4.2.5. *Relative requirements*

##### Sensitivity and specificity:

During a breast cancer surgery, nonlinear microscopy was used intraoperatively and the images were examined by three pathologists. In this research from Tao et al. they achieved a sensitivity of 95.4% and specificity of 94.1% using SHG(187). In a study on skin lesions by Tsai et al. on skin lesions they were able to reach a sensitivity of 94% and a specificity of 100% using SHG and THG(188). CARS can have a limited sensitivity due to background noise(189). In a study where lung cancer was analysed ex vivo using CARS however, a sensitivity of 91% and a specificity of 92% were reached(190). These results will be different when imaging human brain tissue but they are promising.

Field of view: Since nonlinear microscopy is a microscopic imaging device it is only possible to image structures at a micro and nanoscale, and at a micro or nanoscale resolution. This way it is able to image a network of cells very precisely (175, 191). The required field of view is  $1 \text{ cm}^2$  and so its field of view should be adapted before it can be applied intraoperatively during brain surgery of LGG. The FOV of CARS images are also still too small to use for LGG resection. In this article a FOV of  $50 \mu\text{m}$  is proposed to be ideal for the right spatial resolution (192).

Level of development: SHG, THG and CARS are described as modern microscopic techniques (164). In 1998 THG was first introduced to make dynamic images of living systems. In Squier et al. they used rhizoids from chara plants with cytoplasmic streaming (193). More recent studies researched the applicability of SHG and THG to detect lipid bodies and several cell segments (175, 194, 195). Nowadays it is possible to form good images from subcellular structures as shown in Gavgiotaki et al.

during their research to lipid bodies in microglia cells (175). Research has been showing that TPEF, CARS, SHG and THG are able to image neuronal structures real-time with high resolution, high-contrast, non-invasive, in vivo and label-free. This was tested on rodent brains and in mice where they were able to visualise neuronal structures and micro vessels. The combination of those variants can improve the results (176). In contrast, TPEF, CARS, SHG and THG were able to image neuronal structures in rodent and mice brains with high resolution in vivo, but are not used on tumour tissue yet (176).

Applicability in the OR: Nowadays only experiments with plants and animals are done with THG so it has not been applied in an OR yet (196). Since TPEF, THG and SHG are able to visualise neurodevelopment label-free, in vivo and real-time it is likely that those can be applied in the OR and have improved properties (176). Obtained images contain high contrast and high resolution of the imaged structures in vivo. It is also possible to stain the signals obtained with THG so the contrast will be in colour (176). Ex vivo images of the brain were made with CARS, which showed high contrast between brain tissue and malignant tissue (197). No limitations have been found which suggests that THG, SHG and CARS would not be applicable in the OR.

Implementation into the OR microscope: Since these techniques are a variant of microscopy it is obvious that it can be integrated in a microscope.

#### 4.2.6 Raman Spectroscopy

Raman spectroscopy (RS) is based on the principles of nonlinear microscopy and uses inelastic scattering caused by tissue when it is excited by an external source. A monochromator is used to send monochromatic laser light into the tissue sample that one wants to analysed. This monochromatic light interacts with the tissue, which causes scattering, absorption or reflection.

Scattering in this case means that photons originated from a light source are deviated from their path because of impurities in a sample, which can occur in different ways and directions. The scattered light caused by the tissue is used to analyse its molecular composition (198). Scattered photons with the same wavelength as the light of the monochromator (Rayleigh scattering, or elastic scattering) will be filtered. The small parts with a changed wavelength, caused by excitations (Stokes and anti-Stokes scattering) will be detected (199).

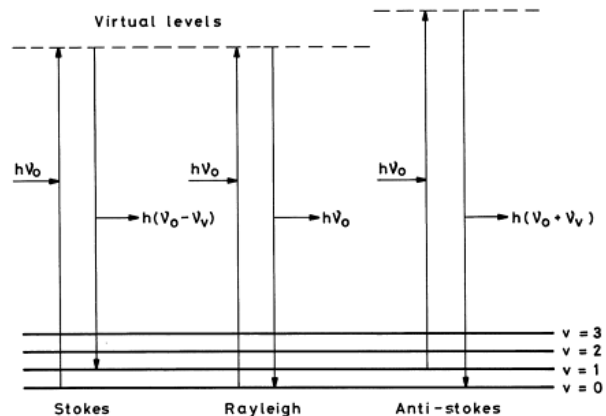


Figure 2: Model of different types of tissue scattering

The different types of scattering are shown in the figure 9. The difference between the wavelength of the lasers and the wavelength of the detected photons equals the energy of the vibrational bonds in molecules that have been excited by the laser. Different molecules will scatter the light in a different way, because each vibrational bond has its own characteristic energy level of the bonds. The energy levels from all kinds of molecule bonds are well defined and so the molecular composition of a sample can be determined. The C-H bonds are most important in RS.

The components a RS system usually consists of are: a laser, a sample illumination system and light collection optics, a wavelength selector (filter) and a detector.

The laser usually uses light with a wavelength of 532 or 785 nm. The light scattered by the tissue is collected by a lens, which can filter Rayleigh scattering. A detector then collects the remaining light followed by extensive processing of the data to obtain a useful RS spectrum. For processing the data, researchers mostly uses Photodiode arrays (PDA) and charge-coupled devices (CCD) (178). Raman scattering on its own is very weak and so there are different ways to enhance the signal (178). CARS for example is introduced to enhance Raman signal as introduced under nonlinear microscopy (177). Furthermore some different variations of Raman will be discussed below.

##### *Stimulated Raman spectroscopy*

Stimulated Raman spectroscopy uses strong laser pulses, instead of a continuous wave laser to illuminate the sample. This results in increased Raman scattering and so a stronger signal is obtained. Up to 50% of the laser energy is transformed into Raman scattering at a Stokes frequency, but only the dominant photons with the Stokes frequency in the scattered light will be amplified. This way the order of magnitude is enhanced 4 to 5 times (200).

##### *Resonance Raman (RR)*

Autofluorescence of a sample due to coloured molecules can contaminate the Raman spectrum, this is a problem especially when UV light is used. Usually these spectra will be filtered and so cannot be detected. Under certain condition however, these auto fluorescent molecules can produce Raman

scattering. Using a laser light with an energy level close to the characteristic energy level from the molecule bonds causes resonance. This principle increases Raman scattering in the order of 3 to 5 times (201).

#### *Surface-Enhanced (Resonance) Raman Spectroscopy (SERS and SERRS)*

SERS and SERRS use the Raman spectra from molecules adsorbed on metal surfaces. This particular form of Raman scattering can be 5 to 6 orders of magnitude stronger than the Raman signal from molecules inside a material, therefore they are adsorbed. Why this works is still a discussion. A disadvantage of SERS is the spectra are difficult to interpret, because of the high number of peaks. Peaks that are usually too small to see can be visualised with SERS and SERRS(200, 202).

Molecular properties of gliomas differ from normal tissue and RS images those properties. This way it is possible to use RS to map those differences, based on the different wavelengths emitted by different molecules in the tissue.

- Lipids: unsaturated lipids between normal tissue and glioma tissue, (and the total amount of lipids was used for grading)(203)
- Proteins(204)
- DNA (205)
- Water contents(206)
- cholesterol and cholesterol esters(204, 205, 207)

#### **4.2.6. Absolute requirements**

Real-time: Up till now RS has been used a little for real time imaging in the OR. Beleites et al. have used a probe with a RS laser to obtain images of low and HGGs. However these images could not be used yet during surgery because they had to be processed first in order to judge the spectra. It took only seconds however to scan spots on the tissue(203). In other studies they used RS to examine tissue samples taken during surgery using neuronavigation. If a larger area can be scanned at the same time, scanning the tissue in real time will be possible.

No brain contact: RS uses a laser to excite the tissue, and the scattered light is collected by a lens, sent through a filter and then analysed. Therefore, images of the brain could be made without making contact. Ex vivo, in a lot of studies RS spectra were acquired without making contact with the tissue, usually using a RS microscope. This proves noncontact images can be made(145, 204, 207). It is possible to obtain data in vivo using RS, but so far optical fibre probes have been used. These probes had to contact the brain tissue(207). A way to make images in vivo without touching the brain has yet to be found, but theoretically it is possible

In vivo imaging: It is possible to acquire data in vivo this was done by Beleites et al. and Jermyn et al. using a RS handheld probe. The RS data was obtained in vivo and later processed(203, 207).

No contrast agent: RS is based on the inelastic scattering of light without the need for a contrast agent. In Jermyn et al. they imaged brain tissue in vivo without a contrast agent(207, 208).

No tissue damage: According to Shenoy et al, RS is a non-destructive way to analyse tissue(208). RS was even used to analyse tissue damage caused by solar radiation and radiotherapy(209, 210). A lot of research has been done using RS, and no tissue damage was ever reported.

#### 4.2.6. *Relative requirements*

High sensitivity and specificity: It is essential that obtained data is reliable, so the right tissue will be labelled as tumour tissue. Most important is no healthy tissue is removed from the brain. In the experiments performed by Jermyn et al. they used RS to find glioma grade II-IV margins beyond the margins visible on the preoperative MRI. The sensitivity was 94% and specificity 86% detecting cancer in all samples (207). These are promising results, but which glioma grades were analysed was not further specified. In another study 135 Raman spectra of nine glioma and normal tissue samples were compared with a sensitivity of 100% and a specificity of 70% (208). This shows the sensitivity of RS is promising but the specificity should be increased, but in this article it was not specified what type of gliomas was used for the experiments.

Applicability in the OR: RS has been used to obtain data during surgery without the need for bulky equipment to produce the images. In the study by Krafft et al. for example tissue samples were obtained during a glioma resection using a RS probe for further investigation(205). The equipment needed for RS will not be a problem to fit in a regular theatre, but there might be some obstacles. The fraction of Raman scattering in the scattered light is very small, which makes it difficult to detect and make an image. Raman scattering is usually 10 order of magnitude smaller than fluorescence(211). This means the lights have to be turned off in order to obtain a spectrum. After data is acquired using a RS laser, it must be processed before the spectra can be analysed. In a study by Barroso et al. RS was used to determine water content in tongue resections looking for squamous cell carcinoma (SCC). After illuminating the samples with an RS laser, the data was analysed calculating an average spectrum for each measurement point, in order to obtain the total Raman spectrum. An image of the tissue was not made, just a spectrum(206).

Field of view: RS is a technique used to visualise molecular properties on a small scale (212). In Lattermann et al. a resolution of 1  $\mu\text{m}$  per pixel was used to obtain the RS images with an FOV of 100  $\mu\text{m}^2$ (213). Using only the laser, a very small part of the tissue is illuminated at the same time. This results in a very small FOV, which makes it difficult to image a big part of the brain at the same time. Line scanning is also possible, and depending on the size of the area scanned the FOV can be enlarged (214). The possibilities of line scanning have to be further investigated.

Implementation into the OR microscope: Often a microscope with an integrated RS laser was used to evaluate tissue samples. In Bergner et al. they used a confocal Raman micro spectrometer coupled to a single mode diode laser (204). In Gajjar et al. they used a Raman Spectrometer with the same type of laser and a white light camera which was built into the microscope (145). This proves RS laser could be built into a microscope. There is not mentioned whether an RS image could be projected into the microscope in any article.

Level of development: RS is an upcoming technique as an addition to histopathology. Recent developments in RS have created the possibility for in vivo imaging (215). Classification models are developed for identification of tissue using probes (216). In Brain tissue, RS already has been applied for in vivo data acquisition of LGGs (203, 207). Real time analysis of the tumours was not possible yet, because the Raman spectra require multivariate algorithms for analysis. Software to apply these algorithms and process data in real time has not been developed yet. This applies to all types of tumours now examined with RS (215). RS probes have been developed for colorectal cancers, but this proves to be difficult (217). Only limited studies have been performed to evaluate the use of RS to diagnose cancers in the gastric system. RS probes have also been used for in vivo imaging of Oesophageal cancers. In Haung et al. they acquired RS spectra of the oesophagus in 0.5 seconds,

however they have not mentioned whether or not the tumours were visible with a white light endoscope (218). Furthermore RS probes have been used to keep an eye on axillary nodes in patients with breast cancer. This was performed on ex vivo samples with a hand held probe (219). Investigation to use RS for in vivo detection of breast cancer is still going on with promising results (215). In bladder diseases RS has often been used in combination with 5-ALA, an application irrelevant for this research paper, but this has been researched for in vivo applications (220). Moreover ex vivo studies for determining cancerous tissue in the bladder wall have been performed (221), but in vivo studies have not yet been carried out.

## 5 Comparison of included imaging techniques

The relative requirements have been compared for all of the techniques and grades have been assigned. Furthermore the requirements are graded in range of importance. Far most important is sensitivity and specificity. The technique should be able to produce reliable results, with as little as possible false positives and false negatives. Otherwise it would create too many risks. This is why sensitivity and specificity weighs 50% in importance. Second important is applicability in the OR. When it appears a technique is not able to be applied in the OR, it is not worth considering. In contrast there should be noted that mostly techniques can be applied in the OR in some way, so the techniques were ranged to what degree it already can be implemented in the OR. Next important requirement is field of view. When a technique is only able to image on cell level, the surgeon will not be able to resect the tumour at tissue level. However, it is possible in some cases to adapt the field of view. That is why it weighs less compared to applicability in OR and sensitivity and specificity. Fourth important is level of development. Level of development is important because higher developed techniques could be easier implemented in the OR and more reliable considerations can be made about its potential. However, this property is not necessary because it is variable and could be improved in time. The last requirement is implementation into the microscope. This requirement is less important because most techniques can be implemented into the OR in some way. The grades for each requirement and the total grade are listed in *table 6* below for each imaging technique. The arguments on which the grades are based are explained below the table.

<i>Relative Requirements</i>	<b>Sensitivity and specificity</b>	<b>Applicability in the OR</b>	<b>Field of view</b>	<b>Level of development</b>	<b>Implementation into the microscope</b>	<b>Total</b>
<i>Techniques</i>						
<i>factor</i>	0.5	0.2	0.13	0.12	0.05	1
<b>OCT</b>	4	7	8	7	10	<b>5.78</b>
<b>OCE</b>	5	6	8	5	5	<b>5.59</b>
<b>RS</b>	8	4	2	9	5	<b>6.39</b>
<b>HSI</b>	7	8	10	7	10	<b>7.74</b>
<b>IRs</b>	7	6	3	3	10	<b>5.95</b>
<b>Nonlinear microscopy</b>	6	7	1	6	10	<b>5.75</b>

Table 6 grading of techniques based on relative requirements

## 5.1 Sensitivity and specificity

Since not all of the researched techniques have been implemented on brain tissue yet, first a distinction should be made between those techniques which have been implemented on brain tissue and those which have not. Furthermore it is more important that a technique can distinguish LGG tissue from healthy tissue, than from HGG. Since the results are obtained using different tissues and settings, the absolute values of sensitivity and specificity cannot be compared to each other. RS, IR-spectroscopy and OCT have already been tested on brain tissue and even on LGGs. RS was used for detecting the margins of gliomas grade II - IV. Margins of HGGs are more diffuse and show similarities to grade II gliomas. This research led to sensitivity of 94% and a specificity of 86%. Based on these results there can be concluded that RS is promising in detecting LGGs with high accuracy (207). In another study where glioma and normal tissue samples were compared with RS, sensitivity and specificity of 100% and 70% respectively were found (208). RS can distinguish LGG tissue from normal brain tissue with the highest sensitivity and specificity; hence it deserves the highest ranking. IR spectroscopy could distinguish HGG specimens from low grade specimens with a sensitivity of 100% and a specificity of 96.6% (159). Furthermore, IR-spectra from 5 samples of grade II astrocytoma showed significant differences compared to normal brain tissue (160). Using distinction based on architectural changes in *en-face* OCT scans was able to image high-grade glioma, but was not reliable for low-grade gliomas (100). Distinction of diffuse HGG tissue and normal brain tissue based on attenuation coefficient led to a sensitivity of 60% and specificity of 75% (106). OCE, HSI and nonlinear microscopy are left to consider and have not been used on brain tissue samples yet. Since HSI uses light between 400 and 1000 nm, it uses a comparable but also more extended range as IR-spectroscopy. This way its sensitivity and specificity should also be comparable to IR-spectroscopy and maybe even better since its range is more extended. This is the reason why HSI and IR spectroscopy are considered to have an equal sensitivity and specificity (51). OCE provides contrast based on the same principle as shear wave elastography and shear wave elastography has shown stiffer tissue in LGG compared to healthy brain tissue. This way OCE seems promising in detecting LGG tissue (32). Furthermore OCE enables high SNR detection of the nanometre tissue deformation (126). High OCT SNR is required for a high sensitivity. However, this is hard to achieve in soft tissue and highly scattering tissues (107). The sensitivity and specificity of a OCE system are fundamentally limited by the phase sensitivity of the OCE signal-to-noise ratio (SNR) of the system (121). Although this contradiction implies that OCE could be a reliable technique to detect LGG tissue, it has its limitations. This way OCE is considered to have lower sensitivity than HSI and IR. Since OCE can distinguish LGG and OCT cannot, it is considered to have a higher sensitivity and specificity than OCT. Nonlinear microscopy has reached a high sensitivity and specificity in other experiments to breast cancer, lung cancer and skin cancer during surgery (188, 190). Furthermore it is able to show neuronal structures on a cell level (181). This leads to the expectation that differences between LGG cells and healthy brain cells can be imaged. Since no limitations are known, nonlinear is considered to have a higher sensitivity and specificity than OCE.

## 5.2 Field of view

In order to be able to visualise an entire tumour during surgery, the field of view should at least be 1 cm<sup>2</sup>, with a high resolution. Otherwise the surgeon would not be able to resect on tissue scale. Different FOVs can be achieved with different imaging techniques. In one HSI study a real time FOV with a 7.6 cm diameter was reached, this would be perfect for glioma resection (61). Moreover HSI can achieve a resolution between 3.75 and 10.6 nm in the range of spectra between 400-1000 nm, depending on the used system. The FOV of OCE is the same or higher as OCT, from 0.01 cm<sup>2</sup> up to 1 cm<sup>2</sup>. The spatial resolution is 0.01 mm up to 0.1 mm which is suitable for imaging LGGs. C-scan based OCT can achieve an FOV of 1 mm<sup>2</sup> with a resolution of 10-15 µm. The images can be merged

to acquire an FOV of 1 cm<sup>2</sup>, which is suitable for glioma resections. Both OCE and OCT have suitable FOVs (102). In Lattermann et al. a RS resolution of 1  $\mu\text{m}$  per pixel was used to obtain the RS images with a FOV of 100  $\mu\text{m}^2$  covered (213). However a bigger area could be scanned at the same time using a Raman line scanner. This scanner contains a wide laser and does not require a laser focus (214). Possibilities for this line scanner have to be further investigated. In IR the highest FOV reached was 350X350  $\mu\text{m}$ , which is way too small to use during surgery (153). FTIR has a sample aperture of 10-20  $\mu\text{m}$  which acquires a single cell and large organelle lateral spatial resolution(146). Nonlinear microscopy is used at nano and micro scale with a submicron resolution (191). The FOV of CARS for example is about 50  $\mu\text{m}^2$ , this is even smaller than RS and IR spectroscopy. Because the laser has to be focussed it is difficult to create a larger FOV (192).

### 5.3 Level of development

Level of development is also an important feature in ranking the techniques. Some techniques could be implemented in clinical settings within a relatively short amount of time or have been used for other clinical purposes already, while others are far away from clinical implementation. For comparison, two key points are kept in mind. These points are: application on brain tumour tissue and the possibility of in vivo imaging on humans. The technique with the lowest level of development is IR-spectroscopy. FTIR could distinguish glioblastoma from healthy brain tissue in human cells in vitro (150), but have not been used on tumours in humans yet. In contrast, TPEF, CARS, SHG and THG were able to image neuronal structures in rodent and mice brains with high resolution in vivo, but are not used on tumour tissue yet (176). OCE has a higher level of development compared to the previous techniques, due to promising results in other tumours, for example in breast tissue. The disadvantage is OCE has not been used yet on glioma tissue and the only in vivo research so far with OCE has been the imaging of skin (123). However, OCE is expected to have great potential for imaging LGG based on elastic properties. Still, it has to be developed a lot further before implementation in the clinic is possible. HSI was able to distinguish tumour tissue from healthy tissue in other tissues both in vitro and in vivo (54). Moreover, HSI was able to detect an implanted human glioblastoma in a mouse in vivo (68). OCT is in a higher state of development, since OCT has been applied in human tumour resection in neurosurgery on grade III and IV glioma and could differentiate between areas of tumour and healthy tissue (106). Unfortunately, it is currently not suitable for imaging LGG (100). The technique with the highest level of development is RS. RS could detect human LGGs in vivo, but real time grading was not possible due to limitations in data analysis. Software multivariate analysis to process data real-time has yet to be developed (203, 207).

### 5.4 Applicability in the OR

To compare the different techniques for this application, the ease of use and the possibilities in the OR are explored. Since HSI has already been introduced without limitations and has been proven an helpful tool in the OR, it deserves the highest rating for applicability in the OR (47,60). HSI is followed by OCT, since OCT has already been used intraoperatively and has been implemented in OR-microscopes successfully. Furthermore, it is possible to view the OCT images in a heads-up display(105). The current limitation of OCT is it acquires cross-sectional B-scans. It is hard to determine the exact anatomical position where the scan comes from. Although this could be solved by producing 3D-scans with OCT, this method is not fast enough and is not able to capture motion of surgical instruments(103, 104). Nonlinear microscopy is able to image in vivo structures and physiological processes. Furthermore, it can make images with a high-resolution and a high sensitivity and specificity. Except its FOV, there are no limitations in ease of use during surgery. This is why nonlinear microscopy and OCT are grades equally(173). Since OCE is a technique based on

OCT, OCE has the same advantages and disadvantages as OCT when applied in the OR. An additional disadvantage of OCE is that a mechanical load has to be applied to the brain tissue, which requires more adjustments in the OR microscope. Although IR shows promising results in detecting tumour margins using MATLAB software, it has never been applied in the OR yet. Its main limitation is it has not been able yet to combine noncontact measurements with real-time imaging. Nowadays a probe is required for real-time imaging. This leads to interruption of the surgical procedure so IR received the same ranking as OCE. Since RS signals are very weak, they could be contaminated by the lights in the OR. This makes RS the most difficult to integrate into the OR.

## 5.5 Implementation into the OR-microscope

All subcategories of nonlinear microscopy are microscopic devices already, so they can be implemented into an OR-microscopy easily. Since these already are microscopes, they could be integrated perfectly. Since OCT, HSI and IR have already been implemented into a microscope, these techniques are also perfect (59, 107). RS has also been used as a microscopic technique. However, because of its complicated data processing, it could be more difficult to project an image into the microscope (145). OCE is an imaging device based on OCT. Although OCT can be implemented into a microscope, this will be hard for OCE to realize since it needs to produce a mechanical stimulus to load the tissue (124).

## 6 Experiments

During this research we got the opportunity to run some tests with some of the techniques which did comply to the absolute requirements. OCT, HSI, NIR spectroscopy and fluorescence spectroscopy were available to run some experimental tests on glioma tissue samples. The samples were obtained during brain surgery of an astrocytoma grade II and an oligodendroma grade III. After pathologic examination the samples were formalin fixed. One sample from the LGG and one sample from the HGG were used to run the tests on. The samples were prepared by pinning them on a silicone containing Petri disk. The goal of the experiments is determining whether it is possible to see differences in signals between HGG and LGG tissue. These results cannot confirm whether or not the techniques can distinguish LGG from healthy brain tissue. They can only be used to indicate their potentials.

### 6.1 Optical coherence tomography

#### Theory

OCT is able to discriminate between healthy brain areas, solid tumour and necrosis based on differences in light attenuation and microstructures (106). Light attenuation curve can be calculated from averaging multiple A-scans, which represent the signal intensity as a function of depth. This provides information of the light attenuation characteristics on the tissue. In a homogeneous signal, an attenuation coefficient can be calculated from the linear part of the attenuation curve.

Intraoperative OCT imaging showed a high attenuation coefficient in scarred cortex due to high signal intensity with rapid loss in deeper tissues. Cortex invaded by tumour showed a significantly lower attenuation coefficient. The lowest attenuation coefficient was found in high vascularised tumour with a heterogeneous microstructure (98).

Formalin fixation significantly alters the tissue signal in OCT, disturbing the inherent tissue contrast and depth information (see *figure 10*) (78).

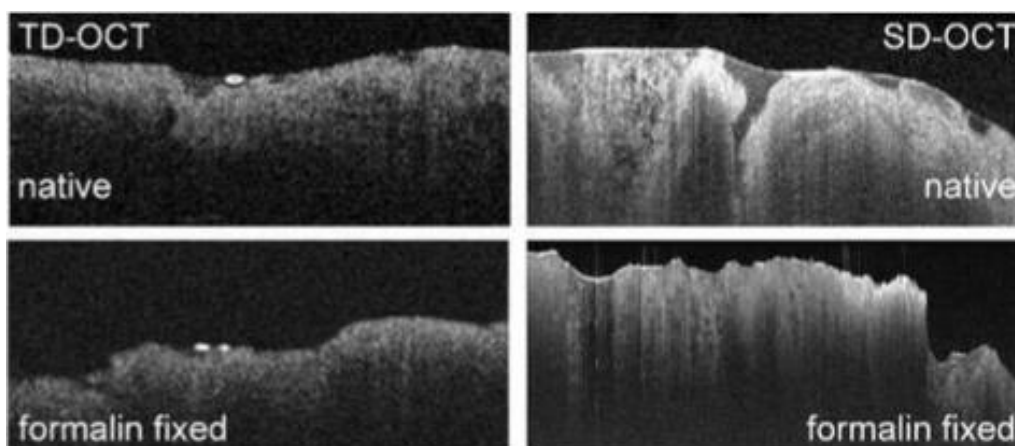


Figure 10 altered tissue signal in OCT due to formalin fixation

## Hypothesis

HGG is more heterogeneous than LGG tissue. Since OCT analysis showed a lower attenuation coefficient in heterogeneous tissue(98). We expect a less rapid loss of signal in HGG than in LGG (106). Although the samples are fixed with formalin, differences in the attenuation curves can be expected (78).

## Method

Samples were analysed with a commercial SS-OCT from Santac, in the setting shown in *figure 12* the lens of the system was set on a focus of 7cm. The laser worked with a central wavelength of 1300 nm, a bandwidth of 100 nm and a sweep rate of 50 kHz. A-scans were selected perpendicular to the tissue surface in multiple slices. These were used to build up B-scans, which were acquired within approximately 2 seconds over the total sample area. Ultimately 3D-scans were obtained containing 1024 x 1024 x 1000 pixels. The 3D-scan could be loaded with Fiji and this way A-scans could be processed using Matlab. To extract the attenuation curves, 20 areas existing of 50 A-scans were selected in both samples (see *figure 11*). This resulted in 2 attenuation curves based on 1000 A-scans which were averaged and plotted in Matlab (Mathworks, inc.) for both samples.



Figure 11 Data selection from B-scans

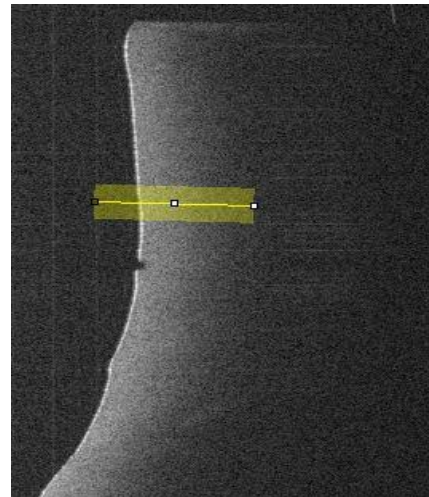


Figure 12 Setting OCT

## Results

In the B-scans of both samples as shown in *figure 13* and *figure 14*, the tissue appeared to be homogeneous. The signal attenuated with a slight slope parallel to the depth of where it came from. Despite a small amount of blood vessels, no significant microstructures were visible.

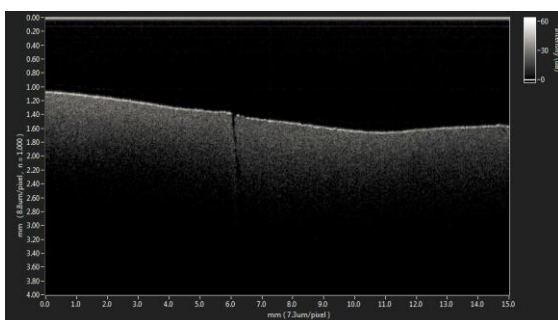


Figure 13 B-scan HGG

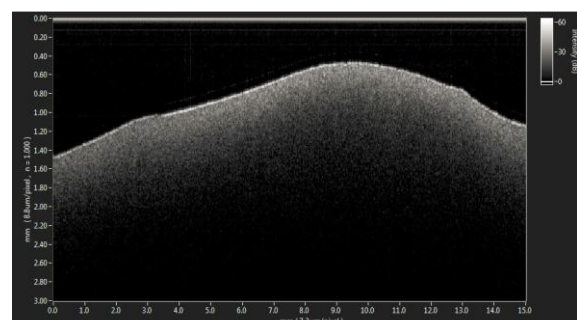
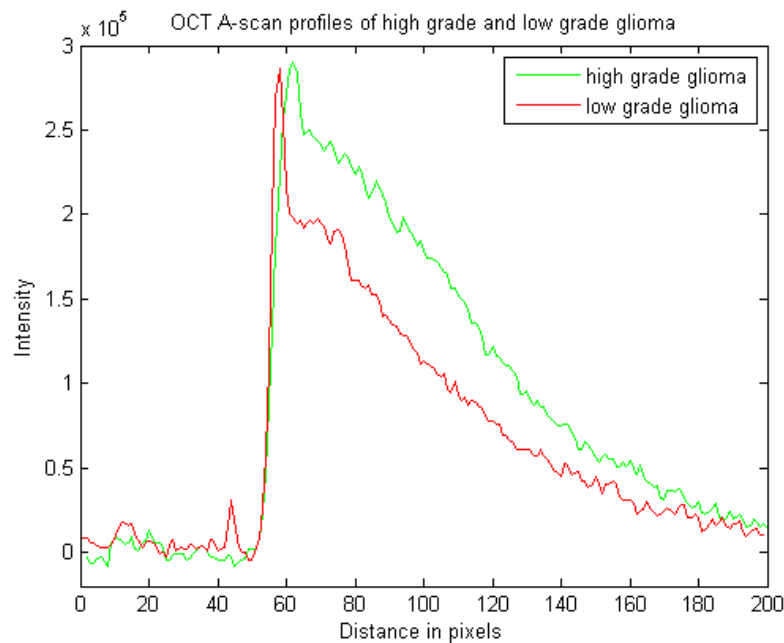


Figure 14 B-scan LGG

The acquired attenuation curves are shown in the *figure 15*. The maximum peaks in both curves represent reflection of light entering the sample and seem to be equal in both samples. The reflectance due to entering the tissue is nearly equal in both samples. However, after entering the sample HGG seems to reflect higher intensities during penetrating the tissue. Moreover in LGG tissue penetration occurs further into the tissue with less reflected intensities.



**Figure 15 Attenuation curves**

### Discussion

*Figure 15* shows the averaged attenuation curves of the HGG (green) and LGG (red). During this experiment 20 areas were selected to analyse. These areas consist of 50 A-scans, representing a relative small amount of total sample volume. Furthermore, only absolute differences between the two samples are considered. Heterogeneous differences within the tissue itself were not taken into account. This way it is hard to conclude whether the higher intensities in HGG is really characteristic for this sample or could also occur within the LGG sample, when selecting other areas. In this experiment 3D data of the sample was acquired in several minutes. To implement OCT during surgery this data acquisition must be real-time and processing has to be achieved within milliseconds. Moreover, a extensive database of the characteristic attenuation values should be composed in order to distinguish LGG with high reliability.

### Conclusion

Based on these graphs there can be concluded that HGG tissue shows higher intensities during penetrating the tissue, when compared to LGG tissue. However when taking into account that little sample areas are selected, it is hard to conclude whether this is really true.

## 6.2 Hyperspectral imaging

### Theory

HSI is based on reflectance intensities of samples. A light source with wavelengths between 400-1000 nm is used to illuminate the brain tissue samples. This light can be absorbed, scattered and reflected by the tissue. HSI detects all spectra of the reflected light from each pixel, to produce a spectrum which contains information about the properties of the sample (47). Since the spectra contain information of visible and not visible light ranges, it acquires extended information compared to the picture which is acquired with HSI. This way HSI is also able to detect properties of the tissue using the near infrared spectrum.

### Hypothesis

Since HGG has higher cell densities compared to LGG and is also less homogeneous tissue, these characteristic properties could show differences in reflectance intensities. This way HGG should create a more irregular reflectance spectrogram compared to LGG (222, 223).

### Method

Formalin fixed HGG (green label) and LGG (red label) were analysed with FTS hyperspectral camera. Each sample was measured twice to detect differences in data analysis during the same sample. The settings are shown in *figure 16*.

Data was processed with Matlab 2014a using application FTS spectral camera. Samples were placed on a white background, which is used as reference. This way it is possible to extract the background data out of the sample data, so only signal emitted by the sample is left. During processing, first obtained HSI image was cropped so less data had to be loaded into the program. Next the background was selected to calculate the reference spectrum. Subsequently ten different regions of each sample were selected, which were automatically corrected for the reference spectrum. These regions were selected relatively on the same spots, when the same sample was loaded from the second analysis. This way differences in one sample could be distinguished.



**Figure 16** Setting of HSI experiment

## Results

### *Astrocytoma grade II*

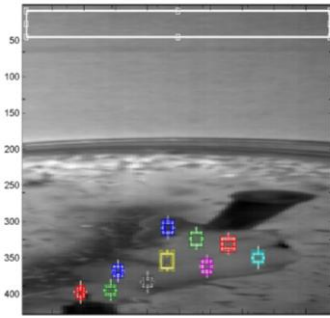


Figure 17 LGG sample 1 with selected region

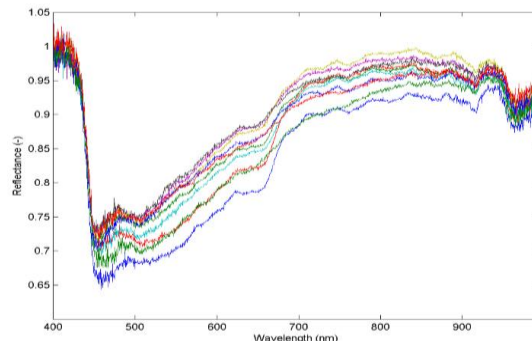


Figure 18 LGG sample 1 spectra of selected region

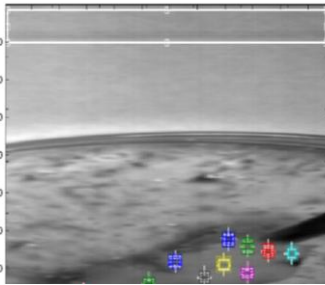


Figure 19 LGG sample 2 with selected regions

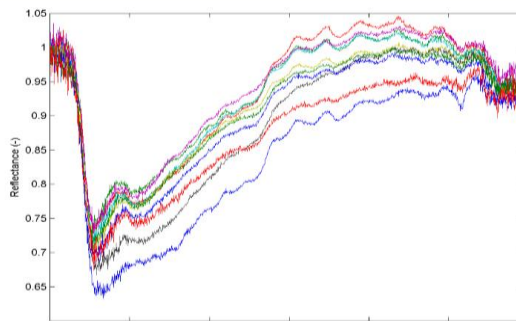


Figure 20 LGG sample 2 spectra of selected regions

### *Oligodendroma grade III*

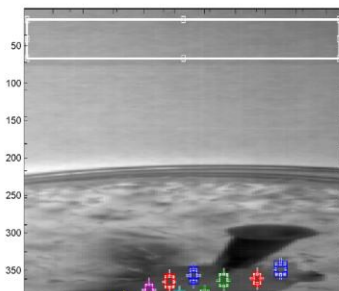


Figure 21 HGG sample 1 with selected regions

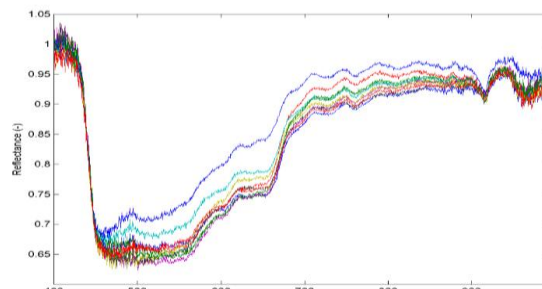


Figure 22 HGG sample 1 spectra of selected regions

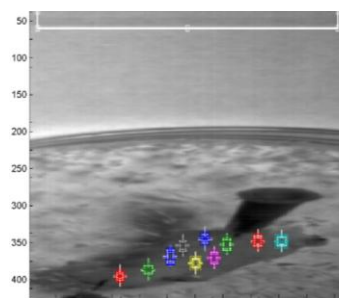


Figure 23 HGG sample 2 with selected regions

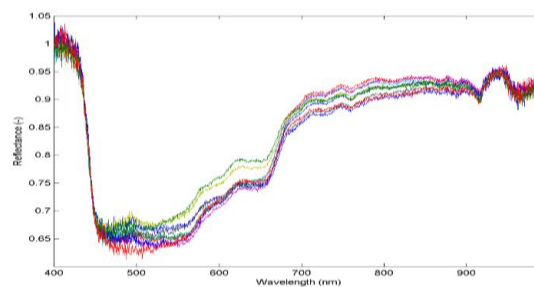


Figure 24 HGG sample 2 spectra of selected regions

The spectra from one sample are comparable between different points. When considering one measurement there should be noted, different spectra are acquired (see *figure 18* and *figure 20*). Although the spectra follow overall comparable courses, it is possible to detect differences in one sample. When comparing the different spectra from both samples (see *figure 18* and *figure 20* and *figure 22* and *figure 24*), the same peaks seem to appear at the same wavelength. For example at 450 nm all the spectra drop from 1 till 0.65, but the HGG drops below 0.65. At 500 nm the LGG shows a peak which is higher than shown in the HGG. At 650 nm troughs are shown which are greater in the HGG. Between 900-1000 nm peaks and troughs are shown in both samples; however these are more accurate in HGG tissue.

### Discussion

It should be noted that HGG tissue shows less differences in the sample, when compared to LGG tissue. This is in conflict with our hypothesis, since we expected more differences in the HGG tissue. This could be caused due to formalin fixation, which results in loss of information (224). Furthermore better conclusions could have been made when it was possible to average the spectra from one sample. The application FTS spectral camera was a fully written script which could not be adapted. This way it was not possible to export the data from the acquired spectra to Matlab or excel and so the spectra could not be averaged. Before HSI can be applied in clinical setting, some adjustments have to be made. For example, during the experiment only an image of the petri-dish with the sample could be acquired. Although this was a real-time image, it took several minutes. Furthermore the acquired hypercube had to be pre-processed before it could be loaded into the written program. This process should be accelerated before it can be used intraoperative. Moreover, regions have to be selected before spectra are acquired and the areas are averaged. When selecting the whole sample, differences in the sample cannot be distinguished anymore. Thus when implementing this technique intraoperative, the spectrum of each pixel should be calculated and in some way translated into an image without the need for region selection.

### Conclusion

HGG tissue shows overall the same courses between different points in the sample. In contrary LGG tissue shows more differences between different points in the sample. When comparing some characteristic peaks, the same peaks are shown in both LGG and HGG tissue. However there are some structural differences between these peaks in high grade and LGG tissue.

## 6.3 Near-infrared spectroscopy

### Theory

In a study by Gajjar et al. FTIR spectroscopy is used to map differences between tumour tissue and normal brain tissue in the 900 to 1800  $\text{cm}^{-1}$  spectral range. The spectra overlap a great deal, but some significant differences can be observed. For example comparable spectral ranges are 1050–1000  $\text{cm}^{-1}$  (carbohydrates and collagen), 1300  $\text{cm}^{-1}$  to 1150  $\text{cm}^{-1}$  (Amide III and PO<sub>2</sub>-) and 1760  $\text{cm}^{-1}$  to 1700  $\text{cm}^{-1}$  (lipids, DNA/RNA and Amide I). The characteristic spectral ranges separating low-grade astrocytoma from healthy brain tissue are shown in *table 7*. These specific spectral ranges allows the identification of molecular markers that can be utilized to separate LGG from healthy brain tissue (145). Extra attention will be paid to these peaks, but other peaks will be analysed as well.

<b><i>Wavenumber (in <math>\text{cm}^{-1}</math>) of different peaks in low grade astrocytoma vs. normal brain tissue</i></b>	<b><i>Molecular marker for this peak</i></b>
<b><i>1103</i></b>	<b><i>No molecular marker</i></b>
<b><i>1234</i></b>	<b><i>nasPO<sub>2</sub>-</i></b>
<b><i>1470</i></b>	<b><i>Lipids</i></b>
<b><i>1504</i></b>	<b><i>Amide II</i></b>
<b><i>1628/1686</i></b>	<b><i>Amide I</i></b>

Table 7 characteristic wavenumbers of astrocytomas

### Hypothesis

Peaks as shown in *table 7* are expected to be found in the glioma tissue used in this experiment as well (145). In this way differences between an anaplastic oligodendroma grade III and a LGG will also be expected to be visible in the spectrum. In wood et al. the influence of formalin was researched using optical imaging devices. Although this research showed differences in tissue scattering, these did not occur in IR-range. This way influence of formalin is not expected during this experiment.

### Method

#### *Data acquisition*

A 1000-1800 nm NIR handheld probe is used to obtain the NIR spectra of the two glioma samples. First, a reference spectrum is made using a reflective material. This serves as reference to show the maximum amount of light which can be reflected and will be used to correct the data. The exposure time is set at 1.3 ms for the reference spectrum. With this exposure time, the highest intensities could be reached, but without saturating the pixels. Next, the measurements of the gliomas were made. The probe is placed on three different spots at each sample. 10 measurements were done at each spot. The three spots chosen on the samples were in both cases on the cortex (grey matter in the edge of the sample), in the middle of the sample (below the cortex) and on the edge across from the first spot. The spots are marked in *figure 25*. During experiments with NIR spectroscopy, the exposure time is usually set at one value during the whole experiment. However, in this experiment, different exposure times were used during the measurements in the cortex (15 ms) and in the white matter (12 ms). No valuable data could be obtained otherwise. This is caused due to less reflection in

the cortex and more reflection in white matter.

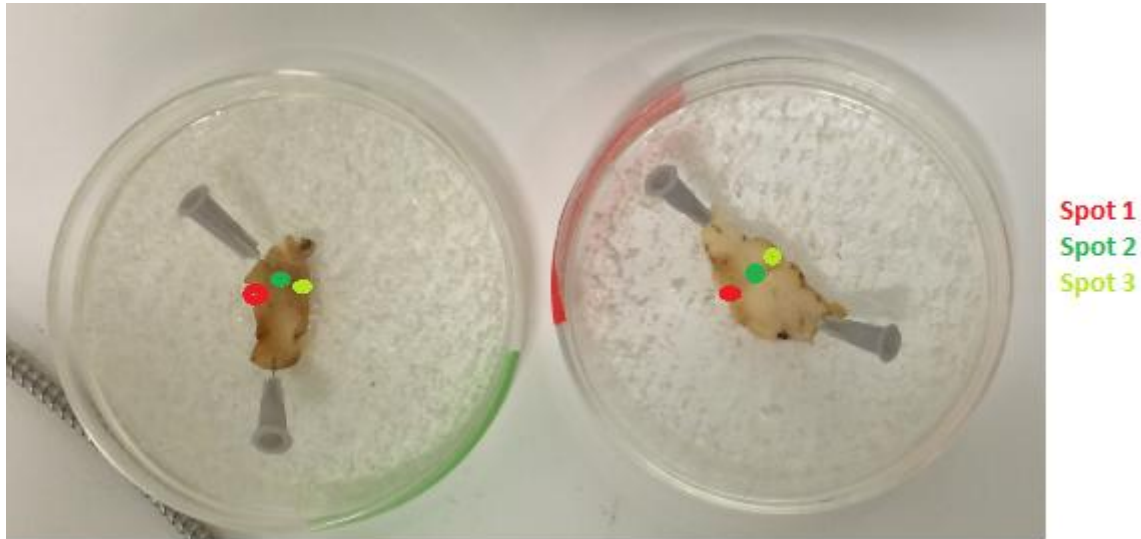


Figure 21 Measuring spots NIR spectroscopy

### Data processing

The 60 tissue measurements and the reference measurement were exported to Microsoft Excel documents during the experiments. First, the ten measurements of each spot were mediated, in order to reduce the standard error. Second, the measurements needed to be corrected by using the reference data. At last, exposure time had to be corrected since this was adapted to each spot. In this way, the spectra of each spot from both samples were acquired

### Results

After data processing, one graph with six spectra (three of each sample) and the reference spectrum was obtained.

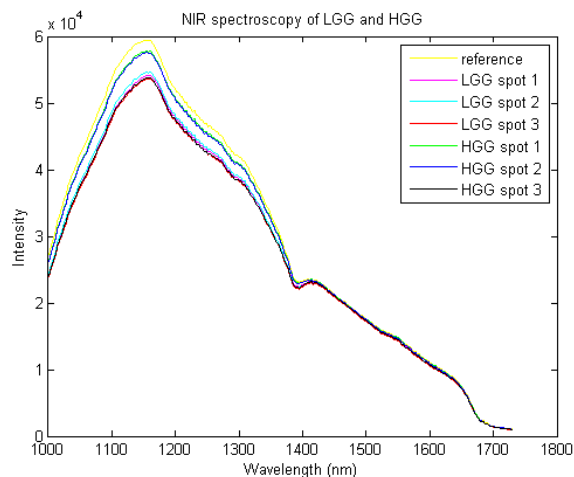


Figure 22 the spectra of the six measuring spots and the reference spectrum, in the 1000-1800 nm area. Spot 1 LGG: cortex . Spot 2 LGG: white matter in the middle. Spot 3 LGG: white matter on the far side of the sample. Spot 1 HGG: cortex. Spot 2 HGG: white matter in the middle. Spot 3 HGG: white matter on the far side of the sample. Reference: the reference spectrum.

Figure 27 shows some overall characteristic peaks at 1158 and 1394 nm. There are no characteristic differences between the spectra of the two samples or with respect to the reference spectrum. Moreover, the peaks as shown in table 7 are absent in all spectra acquired in this experiment.

## Discussion

Since the reference material reflects almost 100% of the light, the reflectance spectra of the samples are expected to be different from the reference peaks. However there is no difference shown between the reference data and experimental data. None of the expected peaks as shown in *table 7* were visible in the spectra of the LGG sample. Furthermore, none of the characteristic diffuse astrocytoma peaks were visible in the LGG, nor were any characteristic peaks in any of the other spectra. It is assumed the differences in the spectral data are too small to be detected with the NIR spectroscopy device we used in this experiment.

During this experiment we experienced a couple of disadvantages of NIR spectroscopy. The probe we used needed to hold still for the acquirement of trustworthy data. The probe also needed to make contact with the sample. This particular form of NIR spectroscopy will not comply with the requirement "no-brain contact". Moreover, only data from one point of the sample could be acquired. NIR spectroscopy used in this way will not be suitable in the OR.

## Conclusion

Since no characteristic peaks are detectable in every graphic, no difference can be made between the different samples or different spots. Even the reference data showed the same characteristic peaks. In this way no relevant data is acquired and no significant conclusions can be made.

## 6.4 Fluorescence spectrometry

### Theory

Fluorescence spectrometry has not been mentioned before in this paper because it is not considered to be applicable in the OR. Among others, it does not comply with the absolute requirements. Since we had the opportunity to use this technique, it seemed useful to compare the outcomes of this experiment with the results of the other experiments anyway. Fluorescence spectrometry uses the interaction of photons with tissue to obtain its signal. A luminescent probe can produce light between 200 and 800 nm with one half of the probe, the other half contains a detector which measures the absorption and reflection of the photons. This results in absorption spectra which contains information about chemical tissue properties (225).

### Hypothesis

Malignancy of glioma is characterised by increased cellularity, vascularisation, endothelial proliferation and necrotic regions (222). These differences should be detected in the absorption spectra of the fluorescence spectrometer. During histopathology it was found that LGG is characterised by honeycomb pattern in oligodendromas, neoplastic astrocytes with losing matrix in astrocytomas and a mixture of these in oligoastrocytomas (223). Since the photon interactions are influenced by cell organelles, these structural changes might also be observed using fluorescence spectroscopy. This should lead to higher intensities detected in oligodendroma tissue due to its heterogeneity, when compared to LGG tissue.

### Method

The samples were analysed with a Perkin Elmer LS55 Fluorescence spectrometer. The sample is placed in a black box to prevent interaction with other light sources, therefore also the room had to be dark. The system sends light with every emission wavelength between 200 and 800 nm and afterwards detects every excitation wavelength. This way it is able to determine the emission and excitation at every wavelength with an acquisition time of approximately 75 minutes. The acquired data is processed with matlab 2014a, resulting in graphics which show the detected intensities at every wavelength.

### Results

#### **HGG**

First order offset: 20

Second order offset: 15

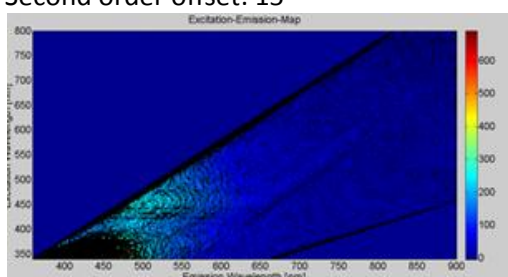


Figure 24 Excitation map of HGG

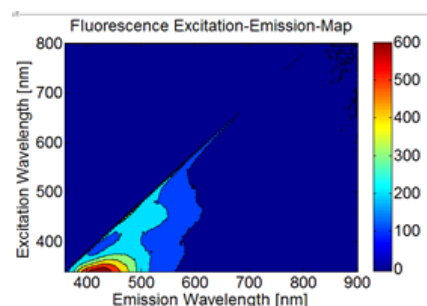


Figure 23 Fluorescence excitation map HGG

## Low grade glioma

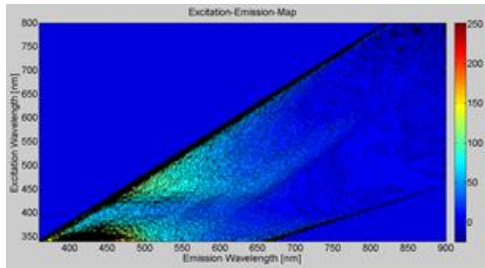


Figure 25 Excitation map of LGG

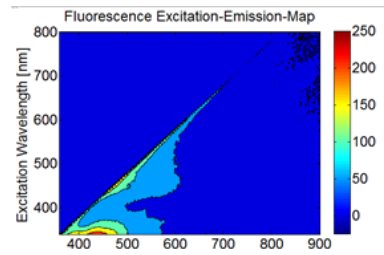


Figure 26 Fluorescence excitation map LGG

These images show the intensities of the emitted light. The first aspect noted is the scale of the color bar. The LGG has an intensity of maximum 250 where HGG shows 600. The highest intensity is both in HGG and LGG between an emission wavelength of 400-500 nm, as best seen in *figure 2* and *figure 4*. This maximum is much higher in HGG than LGG. Furthermore at the excitation wavelength between approximately 400-500 nm, another high intensity is seen in both samples. This maximum is also higher in HGG tissue. However in ratio the intensity is higher in LGG tissue, this is best seen in *figure 1* and *figure 2*. Overall both samples showed intensities between emission and excitation wavelengths of 0-600 nm.

## Discussion

In ratio the intensity at the excitation wavelength between approximately 400-500 nm is higher in LGG. However the intensity bar of the LGG spectrum is lower and so could show more slightly differences. This way, HGG shows possibly the same decay in intensity but this could not be shown as well as by the LGG spectrum. For example an intensity of 100 is shown dark blue in the HGG spectrum but light blue in LGG spectrum. There should be noted, this technique is not considered to be applicable in the OR.

## Conclusion

Characteristic for both samples are higher intensities around excitation and emission wavelengths between 400-500 nm. However these intensities are around 2 to 3 times higher in HGGs. Concluding, HGG tissue shows higher intensities compared to LGG tissue.

## 7 Discussion and conclusion

In this paper, different imaging techniques have been described that might be suitable for intraoperative detection of LGG. In order to select suitable techniques, absolute and relative requirements were determined. The considered techniques had to comply with the absolute requirements, otherwise they were excluded from further investigation. The remaining techniques were graded on a scale from 1 to 10 for each relative requirement, and each requirement got its own scale factor. The scale factors were given based on how important the relative requirements were. This way the potential of each technique was quantified. Aside from literature study, we did some experimental tests with OCT, HSI, fluorescence spectroscopy and NIR-spectroscopy. These were performed to examine whether or not it is possible to see the differences between HGG and LGG tissue *ex vivo*.

Of all imaging techniques in this paper, HSI received the highest mark with a 7.74. HSI received relatively high scores on almost all of the requirements. The most important limitation is HSI has not been applied on brain tissue yet, and the potential of distinguishing LGGs is based on assumptions. However, this applies to more techniques and HSI seems most promising based on the current state-of-the-art.

RS received the second highest grade with a 6.39. This relatively high mark is due to a high level of development and the highest score for sensitivity and specificity. Nevertheless, RS has two major disadvantages: a small FOV and it seems more difficult to apply in the OR than most other techniques. The latter might be a real problem when trying to implement RS for LGG grading and resection. So the high grade which RS received may not entirely condign as a result of mediating.

The mean scores of the other techniques are relatively similar, with grades between 5.59 and 5.95. Despite this similarity, it should be noted the techniques scored very differently on the specific requirements. For example, nonlinear microscopy scored 1 on FOV, while OCT scored an 8. Such a small FOV may raise the question if will ever be suitable for detection of LGGs intraoperatively. If that would be the case, high scores for other requirements would not be relevant anymore, and OCT would actually be far more suitable.

All techniques have different limitations, and different ways of solving those. Some problems might be more difficult to solve than others, which could influence the grading. This is an aspect that has not been taken into account in the comparison of techniques, since no estimation of the difficulty of solving these problems can be made.

The experiments performed in this paper were exploratory. If a technique was able to make a distinction between the HGG sample and the LGG sample, this could be used as an additional recommendation for a technique. However, if no distinction could be made, this could not be used to exclude the technique. There are different reasons why the experiments were not reliable enough to make definite conclusions. The goal of this study is to find a technique able to distinguish LGGs from healthy tissue, but only LGG and HGG samples were available. Therefore it was not possible to determine whether the investigated technique can also distinguish LGG from healthy brain tissue. Furthermore, only one sample of each tumour was tested, and to acquire more reliable results, more samples should be tested. Moreover, the samples were acquired from large tumour resections. Hence, the samples were not fully representative for an entire LGG or HGG. Finally, the data was acquired in *ex vivo* settings, while application would be *in vivo*. *Ex vivo* circumstances are very different from *in vivo* circumstances. For example, the formalin, which is used to fixate the tissue, influences the tissue properties by changing protein structures. This may cause the results of *ex vivo* experiments results to be different from results of *in vivo* experiments.

In conclusion, of all imaging techniques considered in this paper, HSI, RS, OCT, OCE, nonlinear microscopy and IR-spectroscopy seem suitable for intraoperative visualisation of LGGs. Each technique presents its own obstacles, and ongoing developments may lead to the solution of these problems. Based on the requirements, HSI seems most promising.

## 8 References

1. Louis DN, Ohgaki H, Wiestler OD, Cavenee WK, Burger PC, Jouvet A, et al. The 2007 WHO Classification of Tumours of the Central Nervous System. *Acta Neuropathologica* 2007 07/06
2. Louis DN, Perry A, Burger P, Ellison DW, Reifenberger G, von Deimling A, et al. International Society Of Neuropathology--Haarlem consensus guidelines for nervous system tumor classification and grading. *Brain pathology (Zurich, Switzerland)*. 2014 Sep;24(5):429-35.
3. Smoll NR, Gautschi OP, Schatlo B, Schaller K, Weber DC. Relative survival of patients with supratentorial low-grade gliomas. *Neuro-oncology*. 2012;14(8):1062-9.
4. Pouratian N, Asthagiri A, Jagannathan J, Shaffrey ME, Schiff D. Surgery Insight: the role of surgery in the management of low-grade gliomas. *Nature Clinical Practice Neurology*. 2007;3(11):628-39.
5. Van den Bent M, Afra D, De Witte O, Hassel MB, Schraub S, Hoang-Xuan K, et al. Long-term efficacy of early versus delayed radiotherapy for low-grade astrocytoma and oligodendroglioma in adults: the EORTC 22845 randomised trial. *The Lancet*. 2005;366(9490):985-90.
6. Schiff D, Brown PD, Giannini C. Outcome in adult low-grade glioma The impact of prognostic factors and treatment. *Neurology*. 2007;69(13):1366-73.
7. Jakola AS, Myrmet KS, Kloster R, Torp SH, Lindal S, Unsgård G, et al. Comparison of a strategy favoring early surgical resection vs a strategy favoring watchful waiting in low-grade gliomas. *Jama*. 2012;308(18):1881-
8. Meza D, Wang D, Wang Y, Borwege S, Sanai N, Liu JT. Comparing high-resolution microscopy techniques for potential intraoperative use in guiding low-grade glioma resections. *Lasers in surgery and medicine*. 2015 Apr;47(4):289-95.
9. Claes A, Idema A, Wesseling P. Diffuse glioma growth: a guerilla war. *Acta Neuropathologica*. 2007 2007/11/01;114(5):443-58
10. Pallud J, Mandonnet E, Duffau H. Diffuse low-grade gliomas and UCSF scores. *Journal of neurosurgery*. 2014;120(2):577-8.
11. Youland RS, Schomas DA, Brown PD, Nwachukwu C, Buckner JC, Giannini C, et al. Changes in presentation, treatment, and outcomes of adult low-grade gliomas over the past fifty years. *Neuro-Oncology* 2013 06/2
12. Capelle L, Fontaine D, Mandonnet E, Taillandier L, Golmard JL, Bauchet L, et al. Spontaneous and therapeutic prognostic factors in adult hemispheric World Health Organization Grade II gliomas: a series of 1097 cases: clinical article. *Journal of neurosurgery*. 2013;118(6):1157-68.
13. McGirt MJ, Chaichana KL, Attenello FJ, Weingart JD, Than K, Burger PC, et al. Extent of surgical resection is independently associated with survival in patients with hemispheric infiltrating low-grade gliomas. *Neurosurgery*. 2008;63(4):700-8.
14. Smith JS, Chang EF, Lamborn KR, Chang SM, Prados MD, Cha S, et al. Role of extent of resection in the long-term outcome of low-grade hemispheric gliomas. *Journal of clinical oncology : official journal of the American Society of Clinical Oncology*. 2008 Mar 10;26(8):1338-45.
15. Sanai N, Berger MS. Glioma extent of resection and its impact on patient outcome. *Neurosurgery*. 2008;62(4):753-66.
16. Duffau H. The challenge to remove diffuse low-grade gliomas while preserving brain functions. *Acta Neurochir*. 2012 2012/04/01;154(4):569-74. English.

17. Jakola AS, Senft C, Unsgaard G, Solheim O. Surgical management of eloquent supratentorial low-grade gliomas with special emphasis on intraoperative imaging. *Journal of neurological surgery Part A, Central European neurosurgery*. 2015 Mar;76(2):149-59.
18. Nimsky C, Ganslandt O, Hastreiter P, Fahlbusch R. Intraoperative compensation for brain shift. *Surgical neurology*. 2001;56(6):357-64.
19. Stummer W, Pichlmeier U, Meinel T, Wiestler OD, Zanella F, Reulen HJ. Fluorescence-guided surgery with 5-aminolevulinic acid for resection of malignant glioma: a randomised controlled multicentre phase III trial. *The Lancet Oncology*. 2006 May;7(5):392-401.
20. Bernsen H, van der Laak J, Küsters B, van der Ven A, Wesseling P. Gliomatosis cerebri: quantitative proof of vessel recruitment by cooptation instead of angiogenesis. *Journal of neurosurgery*. 2005;103(4):702-6.
21. Barker FG, Chang SM, Huhn SL, Davis RL, Gutin PH, McDermott MW, et al. Age and the risk of anaplasia in magnetic resonance-nonenhancing supratentorial cerebral tumors. *Cancer*. 1997;80(5):936-41.
22. Ricci PE, Dungan DH. Imaging of low- and intermediate-grade gliomas. *Seminars in radiation oncology*. 2001 Apr;11(2):103-12.
23. Kaye AH, Walker DG. Low grade astrocytomas: controversies in management. *Journal of clinical neuroscience*. 2000;7(6):475-83.
24. Khayal IS, VandenBerg SR, Smith KJ, Cloyd CP, Chang SM, Cha S, et al. MRI apparent diffusion coefficient reflects histopathologic subtype, axonal disruption, and tumor fraction in diffuse-type grade II gliomas. *Neuro-oncology*. 2011:nor122.
25. Lee HY, Na DG, Song IC, Lee DH, Seo HS, Kim JH, et al. Diffusion-tensor imaging for glioma grading at 3-T magnetic resonance imaging: Analysis of fractional anisotropy and mean diffusivity. *Journal of Computer Assisted Tomography*. 2008;32(2):298-303.
26. Cha S, Tihan T, Crawford F, Fischbein NJ, Chang S, Bollen A, et al. Differentiation of low-grade oligodendrogliomas from low-grade astrocytomas by using quantitative blood-volume measurements derived from dynamic susceptibility contrast-enhanced MR imaging. *American Journal of Neuroradiology*. 2005;26(2):266-73.
27. Emblem KE, Scheie D, Due-Tonnessen P, Nedregård B, Nome T, Hald JK, et al. Histogram analysis of MR imaging-derived cerebral blood volume maps: Combined glioma grading and identification of low-grade oligodendroglial subtypes. *American Journal of Neuroradiology*. 2008;29(9):1664-70.
28. Maia Jr ACM, Malheiros SMF, Da Rocha AJ, Stávale JN, Guimarães IF, Borges LRR, et al. Stereotactic biopsy guidance in adults with supratentorial nonenhancing gliomas: Role of perfusion-weighted magnetic resonance imaging. *Journal of Neurosurgery*. 2004;101(6):970-6.
29. Law M, Young RJ, Babb JS, Peccerelli N, Chheang S, Gruber ML, et al. Gliomas: Predicting time to progression or survival with cerebral blood volume measurements at dynamic susceptibility-weighted contrast-enhanced perfusion MR imaging. *Radiology*. 2008;247(2):490-8.
30. Caseiras GB, Chheang S, Babb J, Rees JH, Peccerelli N, Tozer DJ, et al. Relative cerebral blood volume measurements of low-grade gliomas predict patient outcome in a multi-institution setting. *European Journal of Radiology*. 2010;73(2):215-20.
31. Hattingen E, Lanfermann H, Quick J, Franz K, Zanella FE, Pilatus U. 1H MR spectroscopic imaging with short and long echo time to discriminate glycine in glial tumours. *Magnetic Resonance Materials in Physics, Biology and Medicine*. 2009;22(1):33-41.

32. Imbault M, Demene C, Mossad M, Gennisson J, Tanter M, Chauvet D, et al., editors. Intraoperative quantitative measurement of brain tumor stiffness and intracranial pressure assessment using ultrasound shear wave elastography. *Ultrasonics Symposium (IUS), 2014 IEEE International*
33. Uzdensky AB, Berezhnaya E, Kovaleva V, Neginskaya M, Rudkovskii M, Sharifulina S. Photodynamic therapy: a review of applications in neurooncology and neuropathology. *Journal of biomedical optics*. 2015 Jun;20(6):61108.
34. Steno A, Karlik M, Mendel P, Cik M, Steno J. Navigated three-dimensional intraoperative ultrasound-guided awake resection of low-grade glioma partially infiltrating optic radiation. *Acta neurochirurgica*. 2012 Jul;154(7):1255-62.
35. Kolkman RG, Blomme E, Cool T, Bilcke M, van Leeuwen TG, Steenbergen W, et al. Feasibility of noncontact piezoelectric detection of photoacoustic signals in tissue-mimicking phantoms. *Journal of biomedical optics*. 2010 Sep-Oct;15(5):055011.
36. Bernsen H, Van der Laak J, Kusters B, Van der Ven A, Wesseling P. Gliomatosis cerebri: quantitative proof of vessel recruitment by cooptation instead of angiogenesis. *Journal of neurosurgery*. 2005 Oct;103(4):702-6.
37. Singh R, Jayanna M, Navadgi S, Ruszkiewicz A, Saito Y, Uedo N. Narrow-band imaging with dual focus magnification in differentiating colorectal neoplasia. *Digestive endoscopy : official journal of the Japan Gastroenterological Endoscopy Society*. 2013 May;25 Suppl 2:16-20.
38. Sasagawa Y, Akai T, Nakada S, Minato H, Tachibana O, Nojima T, et al. Narrow band imaging-guided endoscopic biopsy for intraventricular and paraventricular brain tumors: clinical experience with 14 cases. *Acta neurochirurgica*. 2014 Apr;156(4):681-7
39. Kara MA, Peters FP, Fockens P, ten Kate FJ, Bergman JJ. Endoscopic video-autofluorescence imaging followed by narrow band imaging for detecting early neoplasia in Barrett's esophagus. *Gastrointestinal endoscopy*. 2006 Aug;64(2):176-85
40. Pawley J. *Handbook of Biological Confocal Microscopy*: Springer US; 2010.
41. Gerger A, Hofmann-Wellenhof R, Samonigg H, Smolle J. In vivo confocal laser scanning microscopy in the diagnosis of melanocytic skin tumours. *The British journal of dermatology*. 2009 Mar;160(3):475-81.
42. Eschbacher J, Martirosyan NL, Nakaji P, Sanai N, Preul MC, Smith KA, et al. In vivo intraoperative confocal microscopy for real-time histopathological imaging of brain tumors. *Journal of neurosurgery*. 2012 Apr;116(4):854-60.
43. Lostun D, Perez CJ, Licence P, Barrett DA, Ifa DR. Reactive DESI-MS Imaging of Biological Tissues with Dicationic Ion-Pairing Compounds. *Analytical Chemistry*. 2015 2015/03/17;87(6):3286-93.
44. Calligaris D, Caragacianu D, Liu X, Norton I, Thompson CJ, Richardson AL, et al. Application of desorption electrospray ionization mass spectrometry imaging in breast cancer margin analysis. *Proceedings of the National Academy of Sciences*. 2014 October 21, 2014;111(42):15184-9.
45. Wiseman JM, Ifa DR, Song Q, Cooks RG. Tissue Imaging at Atmospheric Pressure Using Desorption Electrospray Ionization (DESI) Mass Spectrometry. *Angewandte Chemie International Edition*. 2006;45(43):7188-92.
46. Calligaris D, Norton I, Feldman DR, Ide JL, Dunn IF, Eberlin LS, et al. Mass spectrometry imaging as a tool for surgical decision-making. *Journal of mass spectrometry : JMS*. 2013 Nov;48(11):1178-87.

47. Lim HT, Murukeshan VM. Pushbroom hyperspectral imaging system with selectable region of interest for medical imaging. *Journal of Biomedical Optics*. 2015;20(4).
48. Calin MA, Parasca SV, Savastru D, Manea D. Hyperspectral Imaging in the Medical Field: Present and Future. *Applied Spectroscopy Reviews*. 2013 2014/08/18;49(6):435-47.
49. Gat N, editor *Imaging spectroscopy using tunable filters: a review*2000.
50. Panasyuk SV, Yang S, Faller DV, Ngo D, Lew RA, Freeman JE, et al. Medical hyperspectral imaging to facilitate residual tumor identification during surgery. *Cancer biology & therapy*. 2007 Mar;6(3):439-46.
51. Calin MA, Parasca SV, Savastru R, Manea D. Characterization of burns using hyperspectral imaging technique - a preliminary study. *Burns : journal of the International Society for Burn Injuries*. 2015 Feb;41(1):118-24
52. Vo-Dinh T. *Biomedical Photonics Handbook, Second Edition: Biomedical Diagnostics*: Taylor & Francis; 2014.
53. Schumann LW, Lomheim TS, editors. *Infrared hyperspectral imaging Fourier transform and dispersive spectrometers: comparison of signal-to-noise-based performance* 2002
54. Lu G, Fei B. Medical hyperspectral imaging: a review. *Journal of biomedical optics*. 2014;19(1):010901-.
55. Pereira TM, Zezell DM, Bird B, Miljkovic M, Diem M. The characterization of normal thyroid tissue by micro-FTIR spectroscopy. *The Analyst*. 2013 Dec 7;138(23):7094-100.
56. Perez-Guaita D, Heraud P, Marzec KM, de la Guardia M, Kiupel M, Wood BR. Comparison of transfection and transmission FTIR imaging measurements performed on differentially fixed tissue sections. *The Analyst*. 2015 Apr 7;140(7):2376-82.
57. Dedeugd C, Wankhede M, Sorg BS. Multimodal optical imaging of microvessel network convective oxygen transport dynamics. *Applied optics*. 2009 Apr 1;48(10):D187-97.
58. Kim Y-D, Do D, Yoo H, Gweon D. Multimodal confocal hyperspectral imaging microscopy with wavelength sweeping source. *Measurement Science and Technology*. 2015;26(2):025701.
59. Maeder U, Marquardt K, Beer S, Bergmann T, Schmidts T, Heverhagen JT, et al. Evaluation and quantification of spectral information in tissue by confocal microscopy. *Journal of biomedical optics*. 2012 Oct;17(10):106011.
60. Fu D, Xie XS. Reliable Cell Segmentation Based on Spectral Phasor Analysis of Hyperspectral Stimulated Raman Scattering Imaging Data. *Analytical Chemistry*. 2014 2014/05/06;86(9):4115-9.
61. Fu D, Yu Y, Follick A, Currie E, Farese RV, Tsai T-H, et al. In Vivo Metabolic Fingerprinting of Neutral Lipids with Hyperspectral Stimulated Raman Scattering Microscopy. *Journal of the American Chemical Society*. 2014 2014/06/18;136(24):8820-8.
62. Zuzak KJ, Naik SC, Alexandrakis G, Hawkins D, Behbehani K, Livingston EH. Characterization of a Near-Infrared Laparoscopic Hyperspectral Imaging System for Minimally Invasive Surgery. *Analytical Chemistry*. 2007/06/01;79(12):4709-15.
63. Freeman J, Downs F, Marcucci L, Lewis EN, Blume B, Rish J, editors. *Multispectral and hyperspectral imaging: applications for medical and surgical diagnostics*. Engineering in Medicine and Biology Society, 1997 Proceedings of the 19th Annual International Conference of the IEEE; 1997 30 Oct-2 Nov 1997.

64. Khaodhiar L, Dinh T, Schomacker KT, Panasyuk SV, Freeman JE, Lew R, et al. The use of medical hyperspectral technology to evaluate microcirculatory changes in diabetic foot ulcers and to predict clinical outcomes. *Diabetes care*. 2007 Apr;30(4):903-10.
65. Akbari H, Halig LV, Zhang H, Wang D, Chen ZG, Fei B, editors. Detection of cancer metastasis using a novel macroscopic hyperspectral method. *SPIE Medical Imaging; 2012: International Society for Optics and Photonics*.
66. Ferris DG, Lawhead RA, Dickman ED, Holtzapple N, Miller JA, Grogan S, et al. Multimodal hyperspectral imaging for the noninvasive diagnosis of cervical neoplasia. *Journal of Lower Genital Tract Disease*. 2001;5(2):65-72.
67. Hattery D, Hassan M, Demos S, Gandjbakhche A, editors. Hyperspectral imaging of Kaposi's Sarcoma for disease assessment and treatment monitoring. *Applied Imagery Pattern Recognition Workshop, 2002 Proceedings 31st; 2002: IEEE*.
68. Chaudhari AJ, Darvas F, Bading JR, Moats RA, Conti PS, Smith DJ, et al. Hyperspectral and multispectral bioluminescence optical tomography for small animal imaging. *Physics in medicine and biology*. 2005;50(23):5421.
69. Fujimoto JG, Brezinski ME, Tearney GJ, Boppart SA, Bouma B, Hee MR, et al. Optical biopsy and imaging using optical coherence tomography. *Nature medicine*. 1995;1(9):970-2.
70. Fercher A, Mengedocht K, Werner W. Eye-length measurement by interferometry with partially coherent light. *Optics letters*. 1988;13(3):186-8.
71. Huang D, Swanson EA, Lin CP, Schuman JS, Stinson WG, Chang W, et al. Optical coherence tomography. *Science*. 1991;254(5035):1178-81.
72. Walther J, Gaertner M, Cimalla P, Burkhardt A, Kirsten L, Meissner S, et al. Optical coherence tomography in biomedical research. *Analytical and bioanalytical chemistry*. 2011;400(9):2721-43.
73. Podoleanu AG, Seeger M, Dobre GM, Webb DJ, Jackson DA, Fitzke FW. Transversal and longitudinal images from the retina of the living eye using low coherence reflectometry. *Journal of biomedical optics*. 1998;3(1):12-20.
74. Podoleanu AG, Rosen RB. Combinations of techniques in imaging the retina with high resolution. *Progress in retinal and eye research*. 2008;27(4):464-99.
75. Osiac E, Bălșeanu T-A, Cătălin B, Mogoantă L, Gheonea C, Dinescu SN, et al. Optical coherence tomography as a promising imaging tool for brain investigations. *Rom J Morphol Embryol*. 2014;55(2 Suppl):507-12.
76. Drexler W, Morgner U, Kärtner F, Pitris C, Boppart S, Li X, et al. In vivo ultrahigh-resolution optical coherence tomography. *Optics letters*. 1999;24(17):1221-3.
77. Ko T, Adler D, Fujimoto J, Mamedov D, Prokhorov V, Shidlovski V, et al. Ultrahigh resolution optical coherence tomography imaging with a broadband superluminescent diode light source. *Optics Express*. 2004;12(10):2112-9.
78. Böhringer H, Boller D, Leppert J, Knopp U, Lankenau E, Reusche E, et al. Time-domain and spectral-domain optical coherence tomography in the analysis of brain tumor tissue. *Lasers in surgery and medicine*. 2006;38(6):588-97.
79. Häusler G, Lindner MW. "Coherence radar" and "spectral radar" - New tools for dermatological diagnosis. *Journal of Biomedical Optics*. 1998;3(1):21-31.

80. Popescu DP, Flueraru C, Mao Y, Chang S, Disano J, Sherif S, et al. Optical coherence tomography: fundamental principles, instrumental designs and biomedical applications. *Biophysical Reviews*. 2011;3(3):155-69.
81. Liu B, Brezinski ME. Theoretical and practical considerations on detection performance of time domain, Fourier domain, and swept source optical coherence tomography. *Journal of biomedical optics*. 2007;12(4):044007--12.
82. Vakhtin AB, Kane DJ, Wood WR, Peterson KA. Common-path interferometer for frequency-domain optical coherence tomography. *Applied optics*. 2003;42(34):6953-8.
83. Kang J-U, Han J-H, Liu X, Zhang K. Common-path optical coherence tomography for biomedical imaging and sensing. *Journal of the Optical Society of Korea*. 2010;14(1):1-13.
84. Yun S, Tearney G, de Boer J, Iftimia N, Bouma B. High-speed optical frequency-domain imaging. *Optics Express*. 2003;11(22):2953-63.
85. Potsaid B, Baumann B, Huang D, Barry S, Cable AE, Schuman JS, et al. Ultrahigh speed 1050nm swept source/Fourier domain OCT retinal and anterior segment imaging at 100,000 to 400,000 axial scans per second. *Optics Express*. 2010;18(19):20029-48.
86. Bouma BE, Yun S-H, Vakoc BJ, Suter MJ, Tearney GJ. Fourier-domain optical coherence tomography: recent advances toward clinical utility. *Current opinion in biotechnology*. 2009;20(1):111-8.
87. Hwang HS, Shin JG, Lee BH, Eom TJ, Joo C-K. In vivo 3D meibography of the human eyelid using real time imaging Fourier-domain OCT. 2013.
88. Arous JB, Binding J, Léger J-F, Casado M, Topilko P, Gigan S, et al. Single myelin fiber imaging in living rodents without labeling by deep optical coherence microscopy. *Journal of biomedical optics*. 2011;16(11):116012-1160129.
89. Yamashita S, Takubo Y, editors. Wide and fast wavelength-swept fiber lasers based on dispersion tuning for real-time OCT. OFS2014 23rd International Conference on Optical Fiber Sensors; 2014: International Society for Optics and Photonics.
90. Boppart SA, Brezinski ME, Pitris C, Fujimoto JG. Optical coherence tomography for neurosurgical imaging of human intracortical melanoma. *Neurosurgery*. 1998;43(4):834-41.
91. Finke M, Kantelhardt S, Schlaefel A, Bruder R, Lankenau E, Giese A, et al. Automatic scanning of large tissue areas in neurosurgery using optical coherence tomography. *The International Journal of Medical Robotics and Computer Assisted Surgery*. 2012;8(3):327-36.
92. Just T, Lankenau E, Hüttmann G, Pau H. Intra-operative application of optical coherence tomography with an operating microscope. *The Journal of Laryngology & Otology*. 2009;123(09):1027-30.
93. Swanson EA, Izatt J, Lin C, Fujimoto J, Schuman J, Hee M, et al. In vivo retinal imaging by optical coherence tomography. *Optics letters*. 1993;18(21):1864-6.
94. Zhang K, Huang Y, Pradilla G, Tyler B, Kang JU, editors. Real-time intraoperative full-range complex FD-OCT guided cerebral blood vessel identification and brain tumor resection in neurosurgery. SPIE BiOS; 2011: International Society for Optics and Photonics.
95. Tucker-Schwartz J, Meyer T, Patil C, Duvall C, Skala M. In vivo photothermal optical coherence tomography of gold nanorod contrast agents. *Biomedical optics express*. 2012;3(11):2881-95.

96. Au KM, Lu Z, Matcher SJ, Armes SP. Polypyrrole nanoparticles: a potential optical coherence tomography contrast agent for cancer imaging. *Advanced Materials*. 2011;23(48):5792-5.
97. Drexler W, Fujimoto JG. *Optical coherence tomography: technology and applications*: Springer Science & Business Media; 2008.
98. Böhringer H, Lankenau E, Stellmacher F, Reusche E, Hüttmann G, Giese A. Imaging of human brain tumor tissue by near-infrared laser coherence tomography. *Acta neurochirurgica*. 2009;151(5):507-17.
99. Assayag O, Grieve K, Devaux B, Harms F, Pallud J, Chretien F, et al. Imaging of non-tumorous and tumorous human brain tissues with full-field optical coherence tomography. *NeuroImage: Clinical*. 2013 //;2(0):549-57.
100. Assayag O, Grieve K, Devaux B, Harms F, Pallud J, Chretien F, et al. Imaging of non-tumorous and tumorous human brain tissues with full-field optical coherence tomography. *NeuroImage: Clinical*. 2013;2:549-57.
101. Beck JC, Murray JA, Willows AD, Cooper MS. Computer-assisted visualizations of neural networks: expanding the field of view using seamless confocal montaging. *Journal of neuroscience methods*. 2000;98(2):155-63.
102. Assayag O, Antoine M, Sigal-Zafrani B, Riben M, Harms F, Burcheri A, et al. Large field, high resolution full-field optical coherence tomography: a pre-clinical study of human breast tissue and cancer assessment. *Technology in cancer research & treatment*. 2014;13(5):455-68.
103. Binder S, Falkner-Radler CI, Hauger C, Matz H, Glittenberg C. Feasibility of intrasurgical spectral-domain optical coherence tomography. *Retina*. 2011;31(7):1332-6.
104. Ehlers JP, Tao YK, Farsiu S, Maldonado R, Izatt JA, Toth CA. Visualization of real-time intraoperative maneuvers with a microscope-mounted spectral domain optical coherence tomography system. *Retina (Philadelphia, Pa)*. 2013;33(1):232.
105. Tao YK, El-Haddad M, Srivastava S, Feiler D, Noonan A, Rollins A, et al., editors. *Integrative Advances for OCT-Guided Ophthalmic Surgery and Intraoperative OCT*. CLEO: Applications and Technology; 2015: Optical Society of America.
106. Böhringer HJ, Lankenau E, Stellmacher F, Reusche E, Hüttmann G, Giese A. Imaging of human brain tumor tissue by near-infrared laser coherence tomography. *Acta Neurochir*. 2009 2009/05/01;151(5):507-17. English.
107. Ehlers JP, Tao YK, Srivastava SK. The value of intraoperative optical coherence tomography imaging in vitreoretinal surgery. *Current opinion in ophthalmology*. 2014;25(3):221-7.
108. Srinivasan VJ, Wojtkowski M, Witkin AJ, Duker JS, Ko TH, Carvalho M, et al. High-definition and 3-dimensional imaging of macular pathologies with high-speed ultrahigh-resolution optical coherence tomography. *Ophthalmology*. 2006;113(11):2054-65. e3.
109. Kantelhardt SR, Finke M, Schweikard A, Giese A. Evaluation of a completely robotized neurosurgical operating microscope. *Neurosurgery*. 2013;72:A19-A26.
110. Klein T, Wieser W, Eigenwillig CM, Biedermann BR, Huber R. Megahertz OCT for ultrawide-field retinal imaging with a 1050nm Fourier domain mode-locked laser. *Optics Express*. 2011;19(4):3044-62.
111. Schmitt J. OCT elastography: imaging microscopic deformation and strain of tissue. *Optics express*. 1998 Sep 14;3(6):199-211

112. Beer F, Jr. Johnston ER, DeWolf J, Mazurek D. *Mechanics of Materials*: McGraw-Hill Education; 2011.
113. Kennedy KM, Ford C, Kennedy BF, Bush MB, Sampson DD. Analysis of mechanical contrast in optical coherence elastography. *Journal of biomedical optics*. 2013;18(12):121508-.
114. Carcione JM. *Wave fields in real media: Wave propagation in anisotropic, anelastic, porous and electromagnetic media*: Elsevier; 2007.
115. Bedford A, Drumheller DS. *Introduction to Elastic Wave Propagation*: Wiley; 1996.
116. Crecea V, Oldenburg AL, Liang X, Ralston TS, Boppart SA. Magnetomotive nanoparticle transducers for optical rheology of viscoelastic materials. *Optics express*. 2009;17(25):23114-22.
117. Adie SG, Liang X, Kennedy BF, John R, Sampson DD, Boppart SA. Spectroscopic optical coherence elastography. *Optics express*. 2010;18(25):25519-34.
118. Kennedy BF, Kennedy KM, Sampson DD. A review of optical coherence elastography: fundamentals, techniques and prospects. *Selected Topics in Quantum Electronics, IEEE Journal of*. 2014;20(2):272-88.
119. Wang RK, Kirkpatrick S, Hinds M. Phase-sensitive optical coherence elastography for mapping tissue microstrains in real time. *Applied Physics Letters*. 2007;90(16):164105.
120. Li J, Wang S, Singh M, Aglyamov S, Emelianov S, Twa M, et al. Air-pulse OCE for assessment of age-related changes in mouse cornea in vivo. *Laser Physics Letters*. 2014;11(6):065601.
121. Song S, Huang Z, Wang RK. Tracking mechanical wave propagation within tissue using phase-sensitive optical coherence tomography: motion artifact and its compensation. *Journal of biomedical optics*. 2013;18(12):121505-.
122. Li C, Guan G, Huang Z, Johnstone M, Wang R. Noncontact all-optical measurement of corneal elasticity. *Optics letters*. 2012;37(10):1625-7.
123. Kennedy BF, Liang X, Adie SG, Gerstmann DK, Quirk BC, Boppart SA, et al. In vivo three-dimensional optical coherence elastography. *Optics Express*. 2011;19(7):6623-34.
124. Kennedy BF, McLaughlin RA, Kennedy KM, Chin L, Curatolo A, Tien A, et al. Optical coherence micro-elastography: mechanical-contrast imaging of tissue microstructure. *Biomedical optics express*. 2014;5(7):2113-24.
125. Alonso-Caneiro D, Karnowski K, Kaluzny BJ, Kowalczyk A, Wojtkowski M. Assessment of corneal dynamics with high-speed swept source Optical Coherence Tomography combined with an air puff system. *Optics express*. 2011;19(15):14188-99.
126. Wang S, Larin KV. Optical coherence elastography for tissue characterization: a review. *Journal of biophotonics*. 2015 Apr;8(4):279-302.
127. Vakoc B, Yun S, De Boer J, Tearney G, Bouma B. Phase-resolved optical frequency domain imaging. *Optics Express*. 2005;13(14):5483-93.
128. Chau AH, Chan RC, Shishkov M, MacNeill B, Iftimia N, Tearney GJ, et al. Mechanical analysis of atherosclerotic plaques based on optical coherence tomography. *Annals of Biomedical Engineering*. 2004;32(11):1494-503.
129. Dorronsoro C, Pascual D, Pérez-Merino P, Kling S, Marcos S. Dynamic OCT measurement of corneal deformation by an air puff in normal and cross-linked corneas. *Biomedical optics express*. 2012;3(3):473-87.

130. Li X, Li J, Jing J, Ma T, Liang S, Zhang J, et al. Integrated IVUS-OCT imaging for atherosclerotic plaque characterization. *Selected Topics in Quantum Electronics, IEEE Journal of.* 2014;20(2):196-203.
131. Chin L, Kennedy BF, Kennedy KM, Wijesinghe P, Pinniger GJ, Terrill JR, et al. Three-dimensional optical coherence micro-elastography of skeletal muscle tissue. *Biomedical optics express.* 2014;5(9):3090-102.
132. Wang S, Lopez AL, Morikawa Y, Tao G, Li J, Larina IV, et al. Noncontact quantitative biomechanical characterization of cardiac muscle using shear wave imaging optical coherence tomography. *Biomedical optics express.* 2014;5(7):1980-92.
133. Li C, Guan G, Cheng X, Huang Z, Wang RK. Quantitative elastography provided by surface acoustic waves measured by phase-sensitive optical coherence tomography. *Optics letters.* 2012;37(4):722-4.
134. Liang X, Adie SG, John R, Boppart SA. Dynamic spectral-domain optical coherence elastography for tissue characterization. *Optics express.* 2010;18(13):14183-90.
135. Kennedy KM, McLaughlin RA, Kennedy BF, Tien A, Latham B, Saunders CM, et al. Needle optical coherence elastography for the measurement of microscale mechanical contrast deep within human breast tissues. *Journal of biomedical optics.* 2013;18(12):121510-.
136. Wang S, Li J, Manapuram RK, Menodiado FM, Ingram DR, Twa MD, et al. Noncontact measurement of elasticity for the detection of soft-tissue tumors using phase-sensitive optical coherence tomography combined with a focused air-puff system. *Optics letters.* 2012;37(24):5184-6.
137. Schmitt J. OCT elastography: imaging microscopic deformation and strain of tissue. *Optics express.* 1998;3(6):199-211.
138. Flåtten A, Bryhni EA, Kohler A, Egelanddal B, Isaksson T. Determination of C22: 5 and C22: 6 marine fatty acids in pork fat with Fourier transform mid-infrared spectroscopy. *Meat science.* 2005;69(3):433-40.
139. Severcan F, Haris PI. *Vibrational spectroscopy in diagnosis and screening: IOS Press; 2012.*
140. Steiner G, Shaw A, Choo-Smith L, Abuid MH, Schackert G, Sobottka S, et al. Distinguishing and grading human gliomas by IR spectroscopy. *Biopolymers.* 2003;72(6):464-71.
141. McIntosh LM, Jackson M, Mantsch HH, Stranc MF, Pilavdzic D, Crowson AN. Infrared spectra of basal cell carcinomas are distinct from non-tumor-bearing skin components. *Journal of Investigative Dermatology.* 1999;112(6):951-6.
142. Gaigneaux A, Decaestecker C, Camby I, Mijatovic T, Kiss R, Ruyschaert JM, et al. The infrared spectrum of human glioma cells is related to their in vitro and in vivo behavior. *Experimental cell research.* 2004;297(1):294-301.
143. Bi X, Yang X, Bostrom MP, Camacho NP. Fourier transform infrared imaging spectroscopy investigations in the pathogenesis and repair of cartilage. *Biochimica et Biophysica Acta (BBA)-Biomembranes.* 2006;1758(7):934-41.
144. Jiang EY, Rieppo J. Enhancing FTIR imaging capabilities with two-dimensional correlation spectroscopy (2DCOS): A study of concentration gradients of collagen and proteoglycans in human patellar cartilage. *Journal of molecular structure.* 2006;799(1):196-203.
145. Gajjar K, Heppenstall LD, Pang W, Ashton KM, Trevisan J, Patel II, et al. Diagnostic segregation of human brain tumours using Fourier-transform infrared and/or Raman spectroscopy coupled with discriminant analysis. *Analytical Methods.* 2013;5(1):89-102.

146. Baker MJ, Trevisan J, Bassan P, Bhargava R, Butler HJ, Dorling KM, et al. Using Fourier transform IR spectroscopy to analyze biological materials. *Nature protocols*. 2014;9(8):1771-91.
147. Davis BJ, Carney PS, Bhargava R. Theory of mid-infrared absorption microspectroscopy: II. Heterogeneous samples. *Analytical chemistry*. 2010;82(9):3487-99.
148. Perez-Guaita D, Heraud P, Marzec KM, de la Guardia M, Kiupel M, Wood BR. Comparison of transfection and transmission FTIR imaging measurements performed on differentially fixed tissue sections. *Analyst*. 2015;140(7):2376-82.
149. Glassford SE, Byrne B, Kazarian SG. Recent applications of ATR FTIR spectroscopy and imaging to proteins. *Biochimica et Biophysica Acta (BBA)-Proteins and Proteomics*. 2013;1834(12):2849-58.
150. Petibois C, Drogat B, Bikfalvi A, Dél ris G, Moenner M. Histological mapping of biochemical changes in solid tumors by FT-IR spectral imaging. *FEBS letters*. 2007;581(28):5469-74.
151. Pleitez M, Hertzberg O, Bauer A, Seeger M, Lieblein T, Lilienfeld-Toal Hv, et al. Photothermal deflectometry enhanced by total internal reflection enables non-invasive glucose monitoring in human epidermis. *Analyst*. 2015;140(2):483-8.
152. M ller M, Ke ler B. Deposition from dopamine solutions at Ge substrates: An in situ ATR-FTIR study. *Langmuir*. 2011;27(20):12499-505.
153. Bergner N, Romeike BF, Reichart R, Kalff R, Krafft C, Popp J. Tumor margin identification and prediction of the primary tumor from brain metastases using FTIR imaging and support vector machines. *Analyst*. 2013;138(14):3983-90.
154. Yu S, Li D, Chong H, Sun C, Yu H, Xu K. In vitro glucose measurement using tunable mid-infrared laser spectroscopy combined with fiber-optic sensor. *Biomedical optics express*. 2014;5(1):275-86.
155. Chan KA, Kazarian SG. Aberration-free FTIR spectroscopic imaging of live cells in microfluidic devices. *Analyst*. 2013;138(14):4040-7.
156. Goormaghtigh E, Cabiaux V, Ruyschaert J-M. Determination of soluble and membrane protein structure by Fourier transform infrared spectroscopy. *Physicochemical methods in the study of biomembranes*: Springer; 1994. p. 329-62.
157. Gu C, Katti DR, Katti KS. Photoacoustic FTIR spectroscopic study of undisturbed human cortical bone. *Spectrochimica Acta Part A: Molecular and Biomolecular Spectroscopy*. 2013;103:25-37.
158. Fernandez DC, Bhargava R, Hewitt SM, Levin IW. Infrared spectroscopic imaging for histopathologic recognition. *Nature biotechnology*. 2005;23(4):469-74.
159. Sobottka SB, Geiger KD, Salzer R, Schackert G, Krafft C. Suitability of infrared spectroscopic imaging as an intraoperative tool in cerebral glioma surgery. *Analytical and bioanalytical chemistry*. 2009;393(1):187-95.
160. Krafft C, Th mmler K, Sobottka SB, Schackert G, Salzer R. Classification of malignant gliomas by infrared spectroscopy and linear discriminant analysis. *Biopolymers*. 2006;82(4):301-5.
161. Urboniene V, Pucetaite M, Jankevicius F, Zelvy A, Sablinskas V, Steiner G. Identification of kidney tumor tissue by infrared spectroscopy of extracellular matrix. *Journal of biomedical optics*. 2014;19(8):087005-
162. Jonge MD, Martin P. Automated Positioning Meets Microspectrophotometry. *Photonics Spectra*. 2004;38(11):82-3.

163. Noreen R, Chien CC, Chen HH, Bobroff V, Moenner M, Javerzat S, et al. FTIR spectro-imaging of collagen scaffold formation during glioma tumor development. *Analytical and bioanalytical chemistry*. 2013 Nov;405(27):8729-36
164. Vielreicher M, Schürmann S, Detsch R, Schmidt M, Buttgerit A, Boccaccini A, et al. Taking a deep look: modern microscopy technologies to optimize the design and functionality of biocompatible scaffolds for tissue engineering in regenerative medicine. *Journal of the Royal Society Interface*. 2013;10(86):20130263.
165. Ustione A, Piston D. A simple introduction to multiphoton microscopy. *Journal of microscopy*. 2011;243(3):221-6.
166. Yelin D, Silberberg Y. Laser scanning third-harmonic-generation microscopy in biology. *Optics express*. 1999;5(8):169-75.
167. Campagnola PJ, Millard AC, Terasaki M, Hoppe PE, Malone CJ, Mohler WA. Three-dimensional high-resolution second-harmonic generation imaging of endogenous structural proteins in biological tissues. *Biophysical journal*. 2002;82(1):493-508.
168. Mertz J. Nonlinear microscopy: new techniques and applications. *Current opinion in neurobiology*. 2004;14(5):610-6.
169. Chen H, Wang H, Slipchenko MN, Jung Y, Shi Y, Zhu J, et al. A multimodal platform for nonlinear optical microscopy and microspectroscopy. *Optics express*. 2009;17(3):1282-90.
170. Moreaux L, Sandre O, Charpak S, Blanchard-Desce M, Mertz J. Coherent scattering in multi-harmonic light microscopy. *Biophysical Journal*. 2001;80(3):1568-74.
171. Dempsey WP, Fraser SE, Pantazis P. SHG nanoprobe: Advancing harmonic imaging in biology. *BioEssays*. 2012;34(5):351-60.
172. Tilbury K, Campagnola PJ. Applications of Second-Harmonic Generation Imaging Microscopy in Ovarian and Breast Cancer. *Perspectives in medicinal chemistry*. 2015;7:21.
173. Débarre D, Supatto W, Pena A-M, Fabre A, Tordjmann T, Combettes L, et al. Imaging lipid bodies in cells and tissues using third-harmonic generation microscopy. *Nature methods*. 2006;3(1):47-53.
174. Pfeffer CP, Olsen BR, Ganikhanov F, Légaré F. Multimodal nonlinear optical imaging of collagen arrays. *Journal of structural biology*. 2008;164(1):140-5.
175. Gavgiotaki E, Filippidis G, Kalognomou M, Tsouko A, Skordos I, Fotakis C, et al. Third Harmonic Generation microscopy as a reliable diagnostic tool for evaluating lipid body modification during cell activation: The example of BV-2 microglia cells. *Journal of structural biology*. 2015;189(2):105-13.
176. Wu Y, Christensen R, Colón-Ramos D, Shroff H. Advanced optical imaging techniques for neurodevelopment. *Current opinion in neurobiology*. 2013;23(6):1090-7.
177. Müller M, Zumbusch A. Coherent anti-Stokes Raman Scattering Microscopy. *ChemPhysChem*. 2007;8(15):2156-70.
178. Downes A, Elfick A. Raman spectroscopy and related techniques in biomedicine. *Sensors*. 2010;10(3):1871-89.
179. Le TT, Yue S, Cheng J-X. Shedding new light on lipid biology with coherent anti-Stokes Raman scattering microscopy. *Journal of lipid research*. 2010;51(11):3091-102.

180. Evans CL, Xie XS. Coherent anti-Stokes Raman scattering microscopy: chemical imaging for biology and medicine. *Annu Rev Anal Chem.* 2008;1:883-909.
181. Witte S, Negrean A, Lodder JC, de Kock CPJ, Testa Silva G, Mansvelder HD, et al. Label-free live brain imaging and targeted patching with third-harmonic generation microscopy. *Proceedings of the National Academy of Sciences.* 2011 April 12, 2011;108(15):5970-5.
182. Sun C-K, Chu S-W, Chen S-Y, Tsai T-H, Liu T-M, Lin C-Y, et al. Higher harmonic generation microscopy for developmental biology. *Journal of structural biology.* 2004;147(1):19-30.
183. Legesse FB, Medyukhina A, Heuke S, Popp J. Texture analysis and classification in coherent anti-Stokes Raman scattering (CARS) microscopy images for automated detection of skin cancer. *Computerized Medical Imaging and Graphics.* 2015;43:36-43.
184. Witte S, Negrean A, Lodder JC, De Kock CP, Silva GT, Mansvelder HD, et al. Label-free live brain imaging and targeted patching with third-harmonic generation microscopy. *Proceedings of the National Academy of Sciences.* 2011;108(15):5970-5.
185. Wu X, Zhuo S, Chen J, Liu N. Real-time in vivo imaging collagen in lymphedematous skin using multiphoton microscopy. *Scanning.* 2011;33(6):463-7.
186. Gao L, Zhou H, Thrall MJ, Li F, Yang Y, Wang Z, et al. Label-free high-resolution imaging of prostate glands and cavernous nerves using coherent anti-Stokes Raman scattering microscopy. *Biomedical optics express.* 2011;2(4):915-26.
187. Tao YK, Shen D, Sheikine Y, Ahsen OO, Wang HH, Schmolze DB, et al. Assessment of breast pathologies using nonlinear microscopy. *Proceedings of the National Academy of Sciences.* 2014;111(43):15304-9.
188. Tsai M-R, Cheng Y-H, Chen J-S, Sheen Y-S, Liao Y-H, Sun C-K. Differential diagnosis of nonmelanoma pigmented skin lesions based on harmonic generation microscopy. *Journal of biomedical optics.* 2014;19(3):036001-.
189. Boas G. Raman technique: Offers promise for clinical applications. *Biophotonics International.* 2014;21(2):27-8.
190. Gao L, Li F, Thrall MJ, Yang Y, Xing J, Hammoudi AA, et al. On-the-spot lung cancer differential diagnosis by label-free, molecular vibrational imaging and knowledge-based classification. *Journal of biomedical optics.* 2011;16(9):096004--10.
191. Tong L, Cheng J-X. Label-free imaging through nonlinear optical signals. *Materials Today.* 2011;14(6):264-73.
192. Hajek KM, Littleton B, Turk D, McIntyre TJ, Rubinsztein-Dunlop H. A method for achieving super-resolved widefield CARS microscopy. *Optics express.* 2010;18(18):19263-72.
193. Squier J, Muller M, Brakenhoff G, Wilson KR. Third harmonic generation microscopy. *Optics express.* 1998;3(9):315-24.
194. Bautista G, Pfisterer SG, Huttunen MJ, Ranjan S, Kanerva K, Ikonen E, et al. Polarized THG microscopy identifies compositionally different lipid droplets in mammalian cells. *Biophysical journal.* 2014;107(10):2230-6.
195. Lee GG, Lin H-H, Tsai M-R, Chou S-Y, Lee W-J, Liao Y-H, et al. Automatic cell segmentation and nuclear-to-cytoplasmic ratio analysis for third harmonic generated microscopy medical images. *Biomedical Circuits and Systems, IEEE Transactions on.* 2013;7(2):158-68.

196. Farrar MJ, Wise FW, Fetcho JR, Schaffer CB. In vivo imaging of myelin in the vertebrate central nervous system using third harmonic generation microscopy. *Biophysical journal*. 2011;100(5):1362-71.
197. Romeike BF, Meyer T, Reichart R, Kalff R, Petersen I, Dietzek B, et al. Coherent anti-Stokes Raman scattering and two photon excited fluorescence for neurosurgery. *Clinical neurology and neurosurgery*. 2015;131:42-6.
198. Bohren CF, Huffman DR. Absorption and scattering of light by small particles: John Wiley & Sons; 2008.
199. Colthup N. Introduction to infrared and Raman spectroscopy: Elsevier; 2012.
200. White JC. Stimulated raman scattering. Tunable lasers: Springer; 1987. p. 115-207.
201. Hu S, Smith KM, Spiro TG. Assignment of protoheme resonance Raman spectrum by heme labeling in myoglobin. *Journal of the American Chemical Society*. 1996;118(50):12638-46.
202. Xu X, Li H, Hasan D, Ruoff RS, Wang AX, Fan D. Near-Field Enhanced Plasmonic-Magnetic Bifunctional Nanotubes for Single Cell Bioanalysis. *Advanced Functional Materials*. 2013;23(35):4332-8.
203. Beleites C, Geiger K, Kirsch M, Sobottka SB, Schackert G, Salzer R. Raman spectroscopic grading of astrocytoma tissues: using soft reference information. *Analytical and bioanalytical chemistry*. 2011;400(9):2801-16.
204. Bergner N, Krafft C, Geiger KD, Kirsch M, Schackert G, Popp J. Unsupervised unmixing of Raman microspectroscopic images for morphochemical analysis of non-dried brain tumor specimens. *Analytical and bioanalytical chemistry*. 2012;403(3):719-25.
205. Krafft C, Belay B, Bergner N, Romeike BF, Reichart R, Kalff R, et al. Advances in optical biopsy– correlation of malignancy and cell density of primary brain tumors using Raman microspectroscopic imaging. *Analyst*. 2012;137(23):5533-7.
206. Barroso EM, Smits RWH, Bakker Schut T, ten Hove I, Hardillo JA, Wolvius EB, et al. Discrimination between oral cancer and healthy tissue based on water content determined by Raman spectroscopy. *Analytical chemistry*. 2015;87(4):2419-26.
207. Jermyn M, Mok K, Mercier J, Desroches J, Pichette J, Saint-Arnaud K, et al., editors. Intraoperative detection of glioma invasion beyond MRI enhancement with Raman spectroscopy in humans. SPIE BiOS; 2015: International Society for Optics and Photonics.
208. Shenoy M, Hole AR, Shridhar E, Moiyadi AV, Krishna CM, editors. Raman spectroscopy of gliomas: an exploratory study. SPIE BiOS; 2014: International Society for Optics and Photonics.
209. Ali S, Bonnier F, Ptasinski K, Lambkin H, Flynn K, Lyng F, et al. Raman spectroscopic mapping for the analysis of solar radiation induced skin damage. *Analyst*. 2013;138(14):3946-56.
210. Lakshmi RJ, Kartha V, Murali Krishna C, R. Solomon J, Ullas G, Uma Devi P. Tissue Raman spectroscopy for the study of radiation damage: brain irradiation of mice. *Radiation research*. 2002;157(2):175-82.
211. Arora R, Petrov GI, Liu J, Yakovlev VV. Improving sensitivity in nonlinear Raman microspectroscopy imaging and sensing. *Journal of biomedical optics*. 2011;16(2):021114--11.
212. Haka AS, Shafer-Peltier KE, Fitzmaurice M, Crowe J, Dasari RR, Feld MS. Diagnosing breast cancer by using Raman spectroscopy. *Proceedings of the National Academy of Sciences of the United States of America*. 2005;102(35):12371-6.

213. Lattermann A, Matthäus C, Bergner N, Beleites C, Romeike BF, Krafft C, et al. Characterization of atherosclerotic plaque depositions by Raman and FTIR imaging. *Journal of biophotonics*. 2013;6(1):110-21.
214. Qi J, Sudheendran N, Liu C-H, Santos GM, Young ED, Lazar AJ, et al., editors. Raman spectroscopy complements optical coherent tomography in tissue classification and cancer detection. *SPIE BiOS; 2015: International Society for Optics and Photonics*.
215. Kallaway C, Almond LM, Barr H, Wood J, Hutchings J, Kendall C, et al. Advances in the clinical application of Raman spectroscopy for cancer diagnostics. *Photodiagnosis and photodynamic therapy*. 2013;10(3):207-19.
216. Shetty G, Kendall C, Shepherd N, Stone N, Barr H. Raman spectroscopy: elucidation of biochemical changes in carcinogenesis of oesophagus. *British journal of cancer*. 2006;94(10):1460-4.
217. Day J, Bennett R, Smith B, Kendall C, Hutchings J, Meaden G, et al. A miniature confocal Raman probe for endoscopic use. *Physics in medicine and biology*. 2009;54(23):7077.
218. Widjaja E, Zheng W, Huang Z. Classification of colonic tissues using near-infrared Raman spectroscopy and support vector machines. *International journal of oncology*. 2008;32(3):653-62.
219. Horsnell J, Stonelake P, Christie-Brown J, Shetty G, Hutchings J, Kendall C, et al. Raman spectroscopy—a new method for the intra-operative assessment of axillary lymph nodes. *Analyst*. 2010;135(12):3042-7.
220. Grimbergen M, van Swol C, van Moorselaar R, Uff J, Mahadevan-Jansen A, Stone N. Raman spectroscopy of bladder tissue in the presence of 5-aminolevulinic acid. *Journal of Photochemistry and Photobiology B: Biology*. 2009;95(3):170-6.
221. De Jong B, Schut TB, Wolffenbuttel K, Nijman J, Kok D, Puppels G. Identification of bladder wall layers by Raman spectroscopy. *The Journal of urology*. 2002;168(4):1771-8.
222. Nelson SJ, Cha S. Imaging glioblastoma multiforme. *The Cancer Journal*. 2003;9(2):134-45.
223. Forst DA, Nahed BV, Loeffler JS, Batchelor TT. Low-grade gliomas. *The oncologist*. 2014;19(4):403-13.
224. Anand S, Cicchi R, Martelli F, Giordano F, Buccoliero AM, Guerrini R, et al., editors. Effects of formalin fixation on tissue optical properties of in vitro brain samples. *SPIE BiOS; 2015: International Society for Optics and Photonics*.
225. Williams ATR, Winfield SA, Miller JN. Relative fluorescence quantum yields using a computer-controlled luminescence spectrometer. *Analyst*. 1983;108(1290):1067-71.